

Emergent Opportunities with Metallic Alloys: From Material Design to Optical Devices

Tao Gong, Peifen Lyu, Kevin J. Palm, Sarvenaz Memarzadeh, Jeremy N. Munday, and Marina S. Leite*

Metallic nanostructures and thin films are fundamental building blocks for next-generation nanophotonics. Yet, the fixed permittivity of pure metals often imposes limitations on the materials employed and/or on device performance. Alternatively, metallic mixtures, or alloys, represent a promising pathway to tailor the optical and electrical properties of devices, enabling further control of the electromagnetic spectrum. In this Review, a survey of recent advances in photonics and plasmonics achieved using metal alloys is presented. An overview of the primary fabrication methods to obtain subwavelength alloyed nanostructures is provided, followed by an in-depth analysis of experimental and theoretical studies of their optical properties, including their correlation with band structure. The broad landscape of optical devices that can benefit from metallic materials with engineered permittivity is also discussed, spanning from superabsorbers and hydrogen sensors to photovoltaics and hot electron devices. This Review concludes with an outlook of potential research directions that would benefit from the *on demand* optical properties of metallic mixtures, leading to new optoelectronic materials and device opportunities.

devices is the fact that their dielectric function (i.e., permittivity, $\epsilon = \epsilon_1 + i\epsilon_2$) is predefined. Thus, several research groups, including ours, have recently merged two almost orthogonal fields, photonics, and metallurgy, to pursue metallic materials with arbitrary permittivity.^[1–5] Alloying is now a burgeoning framework for achieving materials with engineered optical properties, encompassing both nanostructures and thin films, as will be surveyed in this Review.

Plasmonics exploits the interaction of incident electromagnetic fields with the collective motion of free electrons (plasmons) in metals. This phenomenon confines the electromagnetic fields in close vicinity of the metal interfaces, dramatically enhancing the electrical field intensity surrounding the material.^[6–8] Plasmons can be divided into two categories: surface plasmon polaritons (SPP) that propagate along the metal and dielectric interface, and localized surface

plasmon resonance (LSPR) that are confined in a subwavelength nanostructure. For the latter, their optical scattering or absorption (and/or the nearby dielectrics and semiconductors) can be significantly increased. As a result, these enhancement effects are the underpinnings to a range of novel optical processes, and have found countless applications in photovoltaics,^[9–11] photocatalysis,^[12–14] bio- and chemical-sensing,^[15,16] electro-optical modulation,^[17,18] and superabsorbers.^[19–21] As expected, the features of either type of plasmon are strongly dependent upon the dielectric function of the material, which is somewhat fixed in metals.

Concerning materials, coinage metals, such as Au, Ag, or Cu, are widely used in photonics due to their abundant free electrons and chemical stability.^[1] Other noble metals including

1. Introduction

Metals are amongst the most extensively exploited materials in the history of human civilization. Since the Industrial Revolution, their use has percolated into every aspect of our daily life. Metals were initially utilized in construction and machinery, and the early research in the field has been traditionally limited to their structural and thermal properties. In the last decades the understanding and control of the optical and electrical behavior in metallic materials from the macro- to the nanoscale has enabled its adoption in optoelectronics, medicine, and aerospace, amongst other emerging fields. Yet, a primary constraint for utilizing metallic materials as building blocks in photonic

Dr. T. Gong, P. Lyu, Prof. M. S. Leite
Department of Materials Science and Engineering
University of California
Davis, CA 95616, USA
E-mail: mleite@ucdavis.edu

Dr. T. Gong, Prof. J. N. Munday
Department of Electrical and Computer Engineering
University of California
Davis, CA 95616, USA

 The ORCID identification number(s) for the author(s) of this article can be found under <https://doi.org/10.1002/adom.202001082>.

K. J. Palm
Department of Physics
University of Maryland
College Park, MD 20742, USA

K. J. Palm, S. Memarzadeh
Institute for Research in Electronics and Applied Physics
University of Maryland
College Park, MD 20742, USA

S. Memarzadeh, Prof. J. N. Munday
Department of Electrical and Computer Engineering
University of Maryland
College Park, MD 20742, USA

DOI: 10.1002/adom.202001082

Pt and Pd are also well-known plasmonic materials, particularly promising for applications in photocatalysis.^[22] In the last decade, Al has arisen as an alternative plasmonic material due to its low optical loss spanning the entire NUV–vis–NIR spectrum.^[23,24] Very recently, Mg aroused attention as another promising alternative because of its biodegradability and biocompatibility while retaining the advantages of Al, such as low optical loss, CMOS compatibility, and low cost.^[25,26] Regarding other earth-abundant options, transition metals such as Fe and Ni are conventionally used for magnetic and catalytic applications, yet they have shown promises for certain NIR photonic devices despite the relatively high loss.^[27]

While each of the aforementioned metals have their respective advantages and limitations, they are all bound by their own optical properties. In other words, the well-defined dielectric function of individual metals is a hindrance for achieving *on demand* and customizable optical responses. Alloying, blending of two or more different metal elements at the atomic scale, enables significant tunability to ϵ , beyond that of the individual properties of the constituent metals. As a result, it adds a powerful knob for modulation, and provides a pathway for developing game-changing photonic devices. Here, we select examples of how alloying leads to values of permittivity not achievable by pure metals for the following binary mixtures: Ag–Au, Au–Cu, Cu–Ag, Al–Ag, Al–Mg, Al–Cu, Au–Pd, Fe–Au, Pt–Ni, Ag–Pt, Pd–Cu, Mg–Ca; and the ternary Ag–Au–Cu and Ag–Au–Pd combinations.

In this Review we present a survey of the relevant advances on the burgeoning exploration of metallic alloys, focusing on the fields of plasmonics and nanophotonics. We begin with the introduction of several primary alloy nanostructure fabrication techniques, as opposed to the prototypical colloidal chemical methods. Subsequently, we discuss experimental characterization of the alloys' optical properties and analytical modeling of their dielectric functions. Next, we elucidate how this quantity is correlated underlyingly to other physical mechanisms and processes, such as electronic band structure and hot carrier effect. This section is followed by an overview of a number of rising and fast-evolving applications of metal alloys on the basis of their uniquely tunable optical properties. To conclude, we provide an outlook of potential research directions with respect to currently underexplored applications (e.g., dynamic photonics) and alternative computational approaches (e.g., artificial intelligence) to better guide the rational design of metal alloys. Through machine learning, we anticipate that the permittivity of binary and polyelemental metallic materials could be predicted, which, in turn, would accelerate the design of photonic devices.

2. Fabrication of Metal Alloy Nanostructures

The electromagnetic properties of metals have been explored in depth and utilized in realms such as electrical power transmission, telecommunication, antennas and radars, and artificial dielectrics.^[28–31] However, the frequencies of the electromagnetic waves exploited in most of these early applications either fall in the radio frequency or microwave ranges, restricted by the relatively large dimensions of the initial devices and components. Bulk metals at these large dimensions are generally reflective and lossy at optical frequencies, thus their applications had been

limited in this wavelength range. Yet, with significant advances in manufacturing and nanofabrication technology over the past few decades, the dimensions of devices have been reduced to the micro- and nanoscale. This size reduction allows for fundamentally different interactions between metals and optical fields when compared to their bulk counterparts, thereby opening the doors to new scientific fields, such as nanophotonics.

The optical behaviors of metal alloy nanostructures with subwavelength dimensions are strongly dependent upon their chemical composition, geometry, size, and distribution, all of which can be tailored during the fabrication process. Colloidal synthesis methods in the liquid phase are well researched and are the traditional route for the production of metal alloy nanoparticles. However, chemically synthesized nanostructures often end up covered by different stabilizing species/agents, and the alloys are typically limited to only two or three elements.^[32,33] Here, we shift our focus to selected alternative methods that can mitigate these issues. For each one, we discuss the details regarding the fabrication steps and give at least one example of alloyed nanostructures that can be achieved, along with its advantages and limitations.

2.1. Cosputtering with Thermal Annealing

A scalable and well-known route to obtain metal alloy nanostructures (and thin films) in a large area (wafer size) is cosputtering.^[34,35] An example of this fabrication method used to create Ag–Au nanostructures is shown in **Figure 1a(i)**.^[34] The metals of interest are often deposited on the substrate from the sputtering sources simultaneously. The resulted ultrathin film layer is then annealed in a controlled O₂-free environment to prevent oxidation. During the annealing stage, substantial surface diffusion occurs on the interface between the thin film and the substrate to minimize the energy in the system. This dewetting process enables the formation of 3D (often) hemispheric nanoparticles with 10s to 100s of nanometers (see **Figure 1a(ii)**). To investigate if the particles indeed form a solid solution (mixture), energy dispersive X-ray spectroscopy (EDS) elemental mapping has been performed on an individual site after milling by a Ga⁺ focused ion beam (FIB) (see **Figure 1a(iii)**). The homogeneous distribution of the constituent elements throughout the cross-section confirms the successful alloying of Ag and Au. As expected, the final size and spatial distribution (density) of these nanoparticles are determined by parameters such as (i) the metals involved (compositions and surface diffusion coefficients), (ii) the substrate (cohesion and adhesion between the thin film and the substrate), (iii) the amount of material deposited (film thickness), (iv) annealing temperature and time, and (v) gas flow during the annealing step.^[36] Because of the convoluted contributions from all these factors, the fabricated nanostructures often exhibit imperfect distribution in shapes, sizes, and density, which limits the universality of this method.

In addition to cosputtering, sequential deposition method has been reported to fabricate metal alloy nanoparticles such as Pd–Ag, Pt–Ag, Pt–Ag–Au, and Pd–Ag–Au, where bilayer or multilayer films with thicknesses down to the nanoscale are formed.^[37,38] Through subsequent annealing, the nanoparticles undergo nucleation, grain growth, and final breakdown of the

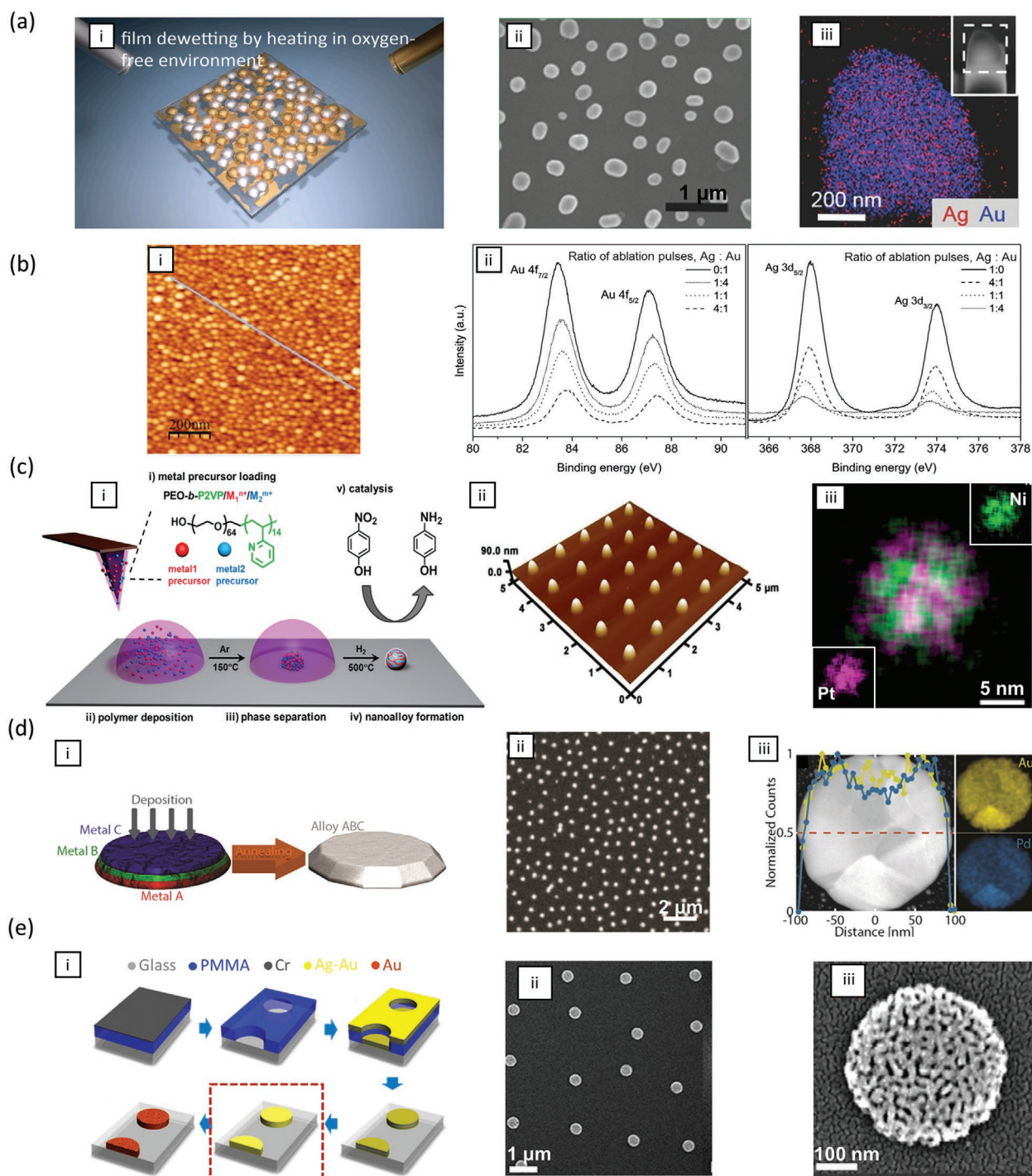


Figure 1. Fabrication methods of metal alloy nanostructures. a) Ag–Au produced by cosputtering deposition followed by thermal annealing. (i) Schematic. Adapted with permission.^[36] Copyright 2019, Elsevier. (ii) Film topography imaged by SEM, (iii) EDS elemental mapping of a representative nanoparticle after center FIB milling. Adapted with permission.^[34] Copyright 2017, Wiley. b) Ag–Au alloys deposited by sequential pulsed laser deposition: (i) AFM topography of nanoparticles under ablation pulse ratio of 1:1. (ii) XPS spectra of Ag:Au alloyed films under ablation pulse ratios of 4:1, 1:1, and 1:4. Adapted with permission.^[40] Copyright 2015, AIP Publishing LLC. c) Alloy nanoparticles generated by SPBCL, a tip-directed synthesis: (i) schematic, (ii) topography of polymer dots imaged by AFM before annealing, and (iii) EDS elemental mapping a single PtNi nanoparticle after annealing. Adapted with permission.^[42] Copyright 2015, American Chemical Society. d) Au–Pd nanodisks fabricated by sequential vapor deposition on HCL mask with thermal annealing. (i) Schematic of multilayer deposition. (ii) SEM image after annealing step, and (iii) HAADF-STEM image with corresponding elemental profile throughout the particle. Adapted with permission.^[3] Copyright 2016, American Chemical Society. e) Nanoporous Au disk fabricated by EBL-based lithography: (i) fabrication schematic of nanodisks highlighting the formation of Au–Ag alloys (red dashed box), SEM images of (ii) arrays, and (iii) an individual nanoparticle where the empty pores illustrate the presence of Ag before a dealloying process. Adapted with permission.^[44] Copyright 2017, American Chemical Society.

large clusters into isolated particles due to the combinational effect of diffusion (inter and surface), Rayleigh instability, and surface energy minimization.^[39] Similarly, this process is highly dependent on temperature, constituents, and thicknesses of the films.

2.2. Sequential Pulsed Laser Deposition

Pulsed laser deposition offers the opportunity of fabricating metal alloy nanostructures in a single step. As described by Verma et al.,^[40] this method utilizes a high-powered pulsed laser beam focused on a metal target in vacuum. The laser vaporizes the metal, which then condenses on the Si substrate and forms a metallic layer. By sequential ablations of different targets, a thin film of densely packed metal alloy nanoparticles can be successfully achieved, as shown in Figure 1b(i). Here, the alloy phase is verified by X-ray photoelectron spectroscopy (XPS), where Ag gains d-band electron charge from Au during annealing,^[41] displaying different intensities at the peaks for varying ablation ratios (see Figure 1b(ii)). The correlation between the ratio of area under the XPS spectra and ablation conditions suggests that the compositions of the alloy films are defined by the ratio of ablation pulses alternating between the metal targets. Therefore, by controlling film thickness, substrate temperature, and metal composition, densely packed alloy nanoparticles can be generated. Nevertheless, the irregular distribution of the nanostructures along with the requirement of high deposition rates makes this method challenging for large-scale production.

2.3. Scanning Probe Block Copolymer Lithography

Although the aforementioned techniques are considered reliable, they do not establish fine control of the size, shape, and position of the final nanoparticles. To overcome these limitations, Chen et al. have proposed a solution called scanning probe block copolymer lithography (SPBCL), which provides precise control of size within a 2–50 nm range.^[42] Figure 1c(i) depicts the SPBCL deposition process. First, a mixed solution of block copolymers, such as poly(ethylene oxide)-*b*-poly(2-vinyl pyridine) (PEO-*b*-P2VP), and metal precursors is loaded onto an atomic force microscope (AFM) probe (or polymer pen tip) and is then deposited on the substrate as an array of polymer dots by scanning the AFM probe (see Figure 1c(ii)). The sample is then annealed in an Ar-environment to promote the aggregation and growth of the metal as a single cluster. The new polymer dots undergo further thermal annealing in H₂ to remove the polymer and excess metal precursors, leaving only one particle at each individual site. The uniform distribution of EDS elemental mapping (see Figure 1c(iii)) proves the formation of an alloyed PtNi nanoparticle. This method can be used for producing multielement alloy systems, with up to five different metals in a single nanostructure. Although SPBCL is a promising approach to fabricate alloy nanoparticles with controlled compositions (determined by the ratio of metal precursors), size (regulated by the amount of polymer loaded on the substrate), and position (easily controlled by the AFM),^[42] it is not suitable for wafer-scale applications.

2.4. Lithography-Based Methods

Lithography-based fabrication routes have the primary advantage of providing very fine control of the geometry, ranging from hollow-squares to triangles, and the spatial distribution of the metallic nanostructures. As known, electron-beam lithography (EBL) enables the formation of structures with subwavelength dimensions down to 20 nm. In this section we discuss two somewhat similar and well-established methods. The first one encompasses the use of tapered nanodisks (see Figure 1d(i)).^[3] Here, the target metals are evaporated sequentially into a prefabricated mask originally made by hole-mask colloidal lithography (HCL).^[43] The chemical composition of the nanostructures is adjusted by careful geometric calculation and precise tracking of the thickness of each metal layer during the physical vapor deposition step. Upon the metal layers deposition, the template is lifted off in acetone. The remaining nanodisks are then thermally annealed in an inert environment for sufficient time to enable atomic mixing of the constituents, resulting in a random array of alloyed nanostructures (see Figure 1d(ii)). The formation of a Au–Pd alloy is verified by high angle annular dark field-scanning transmission electron microscopy (HAADF-STEM), which shows a highly equivalent elemental profile throughout the particle and is further supported by a homogeneous EDS elemental mapping of each metal in an individual nanodisk (see Figure 1d(iii)). To further confirm the generality of this method, a ternary system of Au–Ag–Pd alloy nanodisks was also demonstrated.

The second technique is the conventional electron-beam lithography. As recently shown by Arnob et al., well defined Ag–Au alloy nanodisks are obtained by implementing a process similar to the aforementioned HCL.^[44] The multilayer metallic film is deposited through a mask that is predefined by a focused beam of electrons, and then is thermally annealed after the stripping of the mask (see Figure 1e(i)). Figure 1e(ii) shows a scanning electron microscopy (SEM) overview of a random array of patterned nanodisks. In this specific example, a closer look into the nanostructures, as shown in Figure 1e(iii), reveals the presence of pores, previously occupied by Ag, as a result of a dealloying process.

It should be noted that methods for alloy nanostructure fabrication are rapidly evolving, such as cosputtering followed by sequential ion implantation,^[45] molecular beam epitaxy (MBE),^[46] rapid focused-ion-beam milling-based approach,^[47] carbothermal shock synthesis,^[48] and advanced approaches that integrate lithography with wet-chemistry (e.g., capillary assembly, microcontact printing, dip-pen nanolithography, etc.),^[49] which could enable higher control of material's chemical composition and, therefore, its optical response.

We here emphasize that the fabrication method and condition not only determines the geometry, size, and distribution of the formed nanoparticles, but it also exerts a significant impact on the phase of the resulting alloy systems. As an example, at room temperature, codeposited Au–Cu film is usually disordered as it is stable under equilibrium conditions; yet, annealing causes recrystallization to occur and superlattices can form.^[50] For Ag–Cu a solid solution can be obtained by codeposition at low temperature (≈ 120 K) and subsequent warm-up to room temperature, whereas higher-temperature

annealing would result in impurity clustering and phase separation of the two constituents.^[51] Metastable solutions can also be achieved by high-temperature annealing followed by rapid cooling for some alloys (e.g., Au–Ni).^[52] These examples illustrate well some of the many cases where it is difficult to anticipate when a nanostructure beyond the equilibrium bounds of the composition defined by the pure metals can be achieved. As well documented in the literature,^[53] the phase diagram of the system must be considered.

3. Optical Properties of Metal Alloys

One of the greatest benefits of using metal alloys in photonics is the remarkable tunability of their optical properties. Unlike pure metals whose ϵ is well-defined, alloying could allow for extensive tuning of ϵ by varying their chemical composition. In turn, the mixing of metals can give rise to permittivity values and optical responses that do not exist naturally in pure metals. In this section we review recent investigations of the optical behaviors of different metal alloy systems, and their associated dielectric functions. Further, we emphasize the intrinsic relation between ϵ and the material electronic band structure.

3.1. Optical Extinction Spectra

Optical measurements with alloyed thin films and nanostructures are primarily aimed at understanding how the optical extinction (absorption, reflection, or scattering) varies with the stoichiometry of the metal alloys, which is the basis for their optical tunability. It is important to note that the LSPR of a nanostructure is affected by both chemical composition and their size/geometry. Moreover, as expected, distinct fabrication methods can lead to nanostructures with different shapes and size. Therefore, the comparisons presented in this paragraph refer to samples obtained by the same experimental method and conditions (unless otherwise stated). Nugroho et al.^[3] have compared the optical behaviors of three different binary nanosystems: Au–Ag, Au–Cu, Au–Pd. A monotonical LSPR resonance frequency downshift up to 0.2 eV is observed for the Au–Ag nanodisks with increased Au content, with a slight deviation from the exact linear correlation (see Figure 2a(i),(iv)). But for the Au–Cu alloys, the variation of resonance frequency is much less significant (<0.1 eV) with varying Au content (see Figure 2a(ii),(iv)). Contrastingly, for Au–Pd, a slight addition of Au dramatically reduces the resonance frequency by as much as 0.35 eV with 40% Au content, yet further addition of this metal only causes minimal changes in the resonance frequency (see Figure 2a(iii),(iv)). The resonance linewidth gradually broadens with up to 60% of Au content, but then quickly decreases by 0.3 eV with Au content (see Figure 2a(v)). These LSPR peak shifting behaviors for the Au–Ag and Au–Pd alloy nanoparticles have been affirmed by Kadkhodazadeh et al.^[43] Note that small discrepancies in the exact way the linewidth varies with Au content in the different aforementioned studies are somewhat expected and likely due to the different fabrication conditions used. Rioux et al.^[54] have also reported that the extinction peak wavelength arising from LSPR resonance of 5 nm Au–Ag alloy

nanospheres scales linearly with Au content (see Figure 2b), whereas the resonance linewidth reaches its maximum with a 70% molar fraction of Au. An analogous linear shift of LSPR peak wavelength with increasing Au content in this alloy system has also been reported by Verma et al.^[40] for densely packed nanoparticles. Overall, there is a similar trend for the Ag–Au model system when comparing nanostructures fabricated by the same method: a linear (or almost linear) red shift of the LSPR with the increase of Au. The LSPR peak and width shift is an indication of decent mixing of two metals in the formed particles.

Other than traditional coinage metal-based alloys, studies on earth-abundant and cheaper alternatives are also on the rise.^[55,56] Figure 2c shows the extinction spectra of Al–Mg alloy nanostructures over the entire NUV–vis–NIR wavelength range. The contributions to the total extinction from different metal constituents and respective multipolar scattering are explicitly differentiated. Pure Mg exhibits weak LSPR at long wavelengths (>1 μm) due to relatively high losses,^[26] but the addition of Al to the metal lattice improves the overall resonances in this regime. Although the same fabrication method was implemented for all samples measured, the dipole and quadrupole signatures for the pure Al nanostructure is more pronounced and red shifted. As expected, the extinction for the Mg-rich alloy samples present combined characteristics of both Mg and Al.

In addition, alloying traditional plasmonic metals with transition ones can also reduce cost while maintaining the properties of the transition metal element, such as catalytic activity or magnetism. Amendola et al.^[57] have investigated the plasmonic responses of Fe–Au alloy nanospheres fabricated by laser ablation synthesis in liquid, showing that they display strong attenuation in resonance intensity as the atomic fraction of Fe increases. A small fraction of Fe (10%) quenches the resonance by almost 50% due to the interband transition of electrons from Fe d-states. A slight resonance blueshift from 524 to 506 nm is also observed with increasing Fe content (Figure 2d). Although the plasmonic features are changed, the superparamagnetic nature of Fe in this alloy is largely retained.^[58]

Beyond binary mixtures, multielement alloys can potentially provide even finer control of the overall optical properties as more variables (multielement ratios) are accessible for tuning. As an example, Nugroho et al.^[3] have demonstrated ternary Au–Ag–Pd nanodisks with the extinction spectrum dominated by Pd despite the equal content of all elements. Nevertheless, research on alloys comprising earth-abundant metals and multielement constituents are still at its infancy; therefore, much more remains to be explored. It should be noted that optical responses in all abovementioned systems are not merely a linear combination of those of individual constituents, and macroscopic optical measurements on its own are not sufficient to provide fundamental insight on the origin of their optical behaviors. More in-depth investigation on the dielectric function of the alloys, is required to gain a better understanding of the systems, as will be discussed in the next section.

3.2. Dielectric Functions of Alloys

The macroscopic optical property of a nonmagnetic metal is microscopically determined by its frequency-dependent ϵ ,

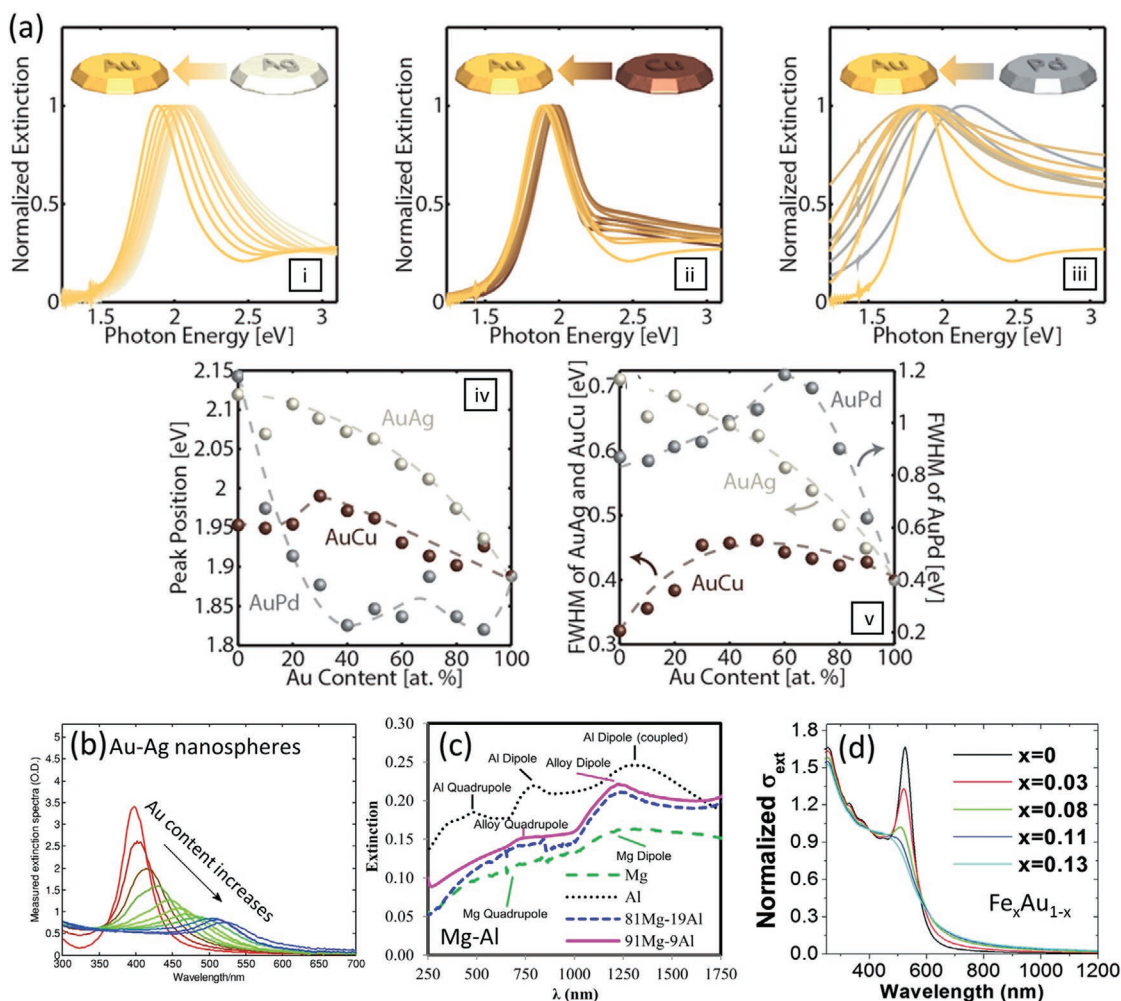


Figure 2. Optical response of metal alloy nanostructures. a) (i)–(iii) Normalized extinction spectra of three different alloy nanodisks: Au–Ag, Au–Cu, and Au–Pd. (iv) Resonance frequency and (v) linewidth shift in each of the three alloys with increasing Au content. Adapted with permission.^[3] Copyright 2016, American Chemical Society. b) Extinction spectra of Au–Ag alloy nanospheres. Adapted with permission.^[54] Copyright 2014, Wiley. c) Extinction spectra of Al–Mg alloy nanoparticles. Adapted with permission.^[55] Copyright 2016, Optical Society of America. d) Normalized extinction cross-section of Fe–Au alloy nanoparticles with varying chemical composition x . Adapted with permission.^[57] Copyright 2014, Royal Society of Chemistry.

which is influenced by a number of features of the material, such as chemical composition, lattice structure, degree of disorder, carrier concentration, and size in the case of nanostructures. As well reported in the literature, with a known dielectric function and a defined size and geometry, the scattering or absorption spectra of a nanostructure can be analytically calculated by Mie theory or numerically simulated by methods such as finite-difference-time-domain, discrete-dipole-approximation, etc.^[59,60] In this section, we summarize experimental and analytical investigations of ϵ for various alloys. We also include recent work that relates it to the electronic band structure of alloyed material.

3.2.1. Experimental Determination of Dielectric Functions

The most common approach to experimentally measure ϵ of a material is variable-angle spectroscopic ellipsometry. Briefly, polarized broadband light is incident on a sample of interest at

multiple angles, and the change of the magnitude and phase of this polarization is measured. For thin films deposited on transparent substrates, transmission measurements are added to provide a more accurate description of ϵ .^[61] The dielectric function of the sample is then retrieved by fitting the experimental transmission and reflection data using fitting models such as B-spline.^[1]

Using ellipsometry, Gong and Leite^[2] have measured ϵ for Ag–Au, Au–Cu, and Cu–Ag alloy thin films with varying chemical composition. A monotonic shift of the threshold wavelength for the interband transition, signified by the abrupt drop of ϵ_2 (see Figure 3a), is observed in the Ag–Au alloy with increasing Au content, resulting from the fact that these metals form a solid solution regardless of their concentration.^[62] This monotonic shift has also been observed by Kadkhodazadeh et al. in an independent study.^[43] By contrast, Au–Cu alloys present a nonmonotonic variation in ϵ_2 (see Figure 3b) due to the presence of nonuniform small grains that enhance light scattering and absorption. In Cu–Ag, two distinct peaks are observed for

ϵ_2 , indicating that the interband transitions in each individual metal contribute independently to the dielectric function (see Figure 3c). This is because, unlike in Ag–Au, Ag, and Cu do not form a solid solution.^[51] Remarkably, it is observed that in all three systems the performance of plasmonic resonances, defined by the SPP quality factor $Q = \epsilon_1^2/\epsilon_2$, can surpass those of individual metals in certain wavelength ranges with particular chemical compositions, corroborating the potential benefits attainable by alloying. In Au–Pd alloys reported by Kadkhodazadeh et al., a 10% addition of Pd to pure Au leads to a substantial increase of ϵ_2 , whereas further incorporation of Pd increases it by a much smaller margin.^[43]

The highly nonlinear relation between the chemical composition and ϵ has been demonstrated in many other alloy systems. Earth-abundant Al–Mg alloys, as reported by Appusamy et al.,^[55] is one example. The Al–Mg thin films are fabricated via cosputtering at room temperature, and a mixture of α -phase solid solution and intermetallic compound phases (β and γ) coexist within the chemical composition range of interest. Figure 3d indicates that Al-rich Al–Mg thin films exhibit higher values of ϵ_2 for wavelengths from 350 to 650 nm than either pure Mg or pure Al. Interestingly, the LSPR quality factor, defined by $Q = |\epsilon_1|/\epsilon_2$, improved in both Al-rich and Mg-rich alloys with modest Mg:Al ratios (35–70%) within the wavelength range of 250–300 nm, as a result of the shift of both ϵ_1 and ϵ_2 . For Al–Ag, the addition of Al up to 12% increases ϵ_2 and slightly blueshifts the interband transition edge. Within this range of Al concentration the alloy is mostly fcc α -phase. Yet, very small fraction of Al (<2%) has negligible effect on its value (see Figure 3e), a manifestation of the nontrivial relation between the composition and the optical property.

In principle, the introduction of one metal element to the other often brings in impurity-induced states and enhances electron scattering in the conduction band. Therefore, for many alloys, the loss (signified by ϵ_2) usually increases compared with their respective constituent metals.^[63,64] However, as seen in the prior examples, ϵ_2 can be contained and suppressed through alloying in certain systems (e.g., Au–Ag, Au–Cu, and Mg–Al) fabricated under specific conditions. Furthermore, another broad class of alloys—the mixing of the coinage metals with other electron-rich ones, may provide a promising pathway to achieve materials with low ϵ_2 . A number of studies have revealed that the extra free-electrons introduced by the metals with high density of carriers (e.g., Cd, Al, Mg, Zn, etc.) can raise the Fermi energy and blueshift the interband transition onset edge, which opens up a frequency range with a much lower ϵ_2 compared to the original coinage metal.^[65] In practice, alloys such as Cu–Al and Au–Cd have been found to exhibit this behavior in the blue-green region of the visible spectrum while the effect is much less profound in other systems.^[66,67]

We note here whilst plasmonics prevalently require a low ϵ_2 , certain optical devices do not. One of the most common examples are the superabsorbers,^[19] which will be discussed in Section 4.1. More recently, the benefits of using ultrathin metallic films to increase light absorption in the NIR range of the electromagnetic spectrum have been demonstrated in systems ranging from hot-carrier devices composed by Si/ultrathin layers of metals and alloys^[27,68] to index-near-zero substrate and

ultrathin metals.^[69] In these devices, the large optical absorption results from the combined effect of large optical attenuation within the lossy thin-film material (e.g., semiconductors or metals) and the nontrivial interface phase shifts.^[70] Overall, the tunability of optical property achieved through alloying, which commonly leads to an increase in ϵ_2 , can be a favorable feature for specific nanophotonic applications.

3.2.2. Analytical Modeling of Dielectric Functions

The most rigorous approach to compute ϵ of a metal or alloy is by first-principles calculation based on time-dependent density functional theory where the response of the electron system to the time-varying electromagnetic perturbation is described fully quantum-mechanically.^[71] In fact, a very recent study has adopted this approach to establish a dielectric function library for binary alloys composed of the common coinage and noble metal constituents.^[72] In this section, however, we concentrate on the modeling of ϵ from the semiclassical perspective, which helps to provide more intuitive and straightforward understanding of the alloy systems.

The dielectric function describes the spatially averaged response of bound and free charges to an exerted optical field in an optically continuous material. In metals, ϵ is typically modeled by the Drude–Lorentz formula^[73,74]

$$\epsilon(\omega) = \epsilon_0(\infty) - \frac{\omega_p^2}{\omega^2 + i\gamma\omega} + \sum_j \frac{f_j}{\omega_{0j}^2 - \omega^2 - i\gamma_j\omega} \quad (1)$$

Here, the first term is the permittivity at infinite frequency, the second one is the well-known Drude term, where ω_p is the plasma frequency (proportional to the free carrier concentration), and the damping frequency γ denotes losses due to intraband transitions. The third term (Lorentzian term) comprises a summation of Lorentz oscillators to account for interband transitions (valence d-band to conduction sp-band) in metals.^[75] The Drude–Lorentz model can be applied to metallic alloys in the same manner as pure metals, and the model parameters can be determined by fitting the experimentally obtained optical data. Hashimoto et al.^[76] have calculated the effective ω_p and damping frequency γ of Au–Ag–Cu ternary alloys with varying Au, Ag, and Cu content. As expected, there is a strong nonmonotonic variation of these parameters with respect to the atomic ratios of the constituents, as displayed in Figure 3f. However the high-quality fit requires an exceedingly large number of Lorentz oscillators (up to 15) to be included, which makes the model somewhat overfit and unphysical, as discussed in other literature.^[54]

As previously stated, ϵ of metallic alloys cannot usually be estimated as a linear combination of its pure constituents weighted by concentration. However, at frequencies where interband transitions do not occur, and in systems where the damping frequencies of the constituent metals are similar, a linear combination works reasonably well (e.g., in Ag–Au for frequencies less than 2 eV).^[40,77] Still, this approximation cannot account for the shift of the interband transition threshold due to the atomic-level mixing of individual metal elements.^[50] Gaudry et al.^[75] have proposed a method to overcome this limitation:

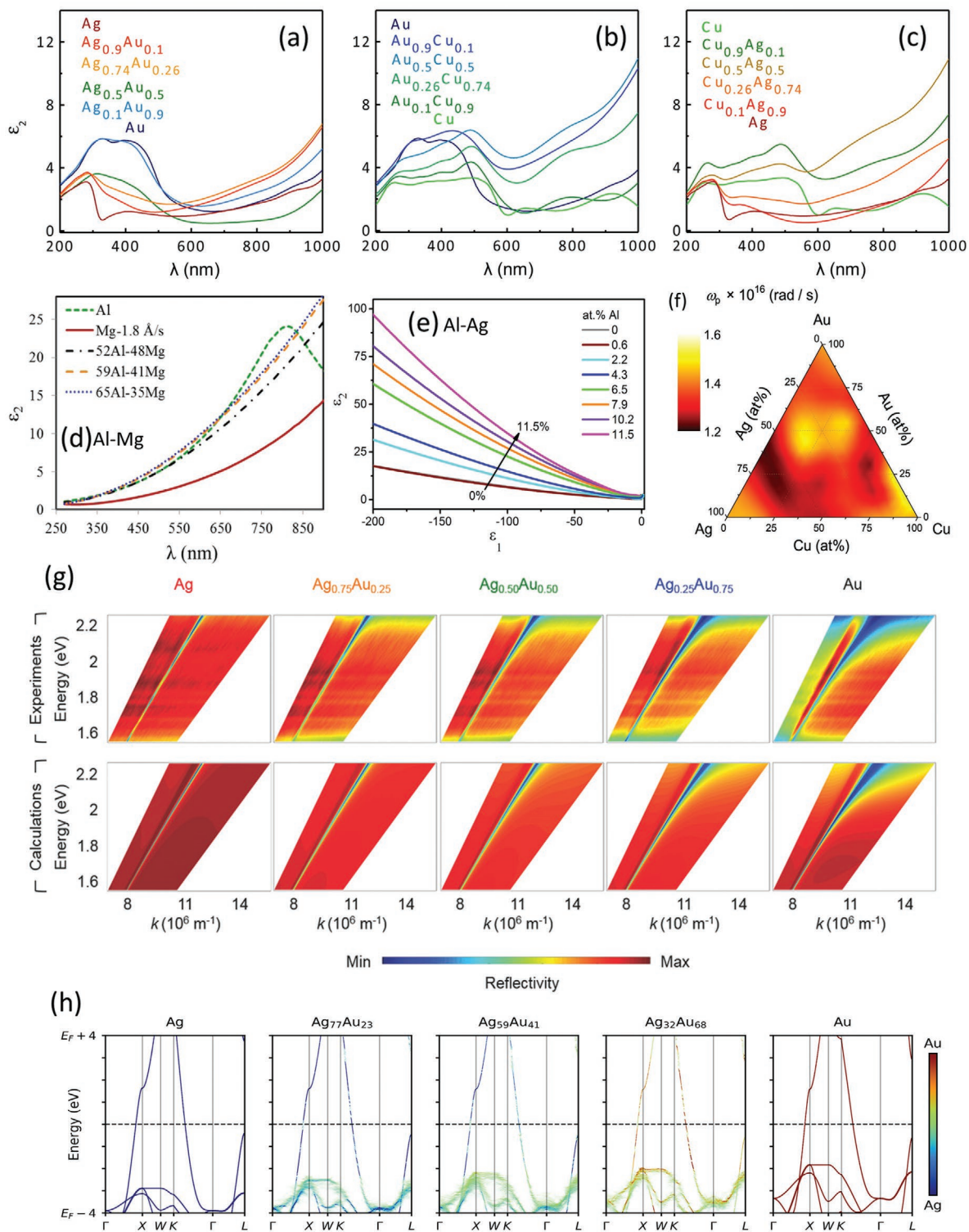


Figure 3. Dielectric function and band structure of metal alloys. Imaginary part of the dielectric function ϵ_2 of binary mixtures of a) Ag–Au, b) Au–Cu, and c) Cu–Ag, and d) Al–Mg alloys as a function of chemical composition. Adapted with permission.^[2] Copyright 2016, American Chemical Society. Adapted with permission.^[5] Copyright 2016, Optical Society of America. e) ϵ_2 as a function of ϵ_1 for Al–Ag thin films. Adapted with permission.^[5] Copyright 2017, IOP Publishing. f) Extracted plasma frequency ω_p of the dielectric function for a ternary Au–Ag–Cu alloy. Adapted with permission.^[76] Copyright 2016, Nature Publishing Group. g) Measured (upper row) and calculated (lower row) reflection spectra-derived SPP dispersion relations for Ag–Au alloy thin films with different Au content. Adapted with permission.^[80] Copyright 2018, Wiley. h) DFT calculated electronic band structures of Ag–Au alloys. Adapted with permission.^[68] Copyright 2020, American Chemical Society.

model the smooth variation of the interband transition edge by a weighted summation of both the interband transition frequencies ω_j and ε_2 of individual metal components in the Lorentzian term. Nevertheless, the analytical model based on the Drude–Lorentz terms can be further refined by incorporating the quantum mechanical aspects of the electronic states of the material, as will be elaborated in the following section.

While the nonlinear variation of ε with alloy's chemical composition enables wide tunability, the resultant optical properties generally do not fall significantly out of the range of the individual constituents. Interestingly, certain intermetallic alloy systems can yield unexpected properties that one hardly realizes through metals or solid solution alloys. Prominent examples are the intermetallic compounds AuAl₂ and PtAl₂. The bulk plasma frequency for these materials reduces from deep UV to 2 and 3 eV, respectively, right within the Vis regime and significantly lower than most metals and alloys.^[78,79] This class of intermetallics further expands the achievable range of dielectric responses, enabling fundamentally different pathways for the improvement of the plasmonic properties and the resultant applications in the optical frequencies.

As mentioned at the beginning of this section, once the dielectric function is determined, the optical behavior of an alloy system can be predicted analytically or numerically and compared with experimental results. As an example, Gong et al.^[80] have measured the reflectivity spectra of coinage alloyed metal thin films using the classical Kretschmann prism coupling configuration specifically designed to compensate for momentum mismatch to excite SPP,^[81] whereby the dip in the reflection spectrum at particular incident angle for each frequency is converted into a dispersion–relation contour of the SPP mode (see Figure 3g upper row). On the other hand, with the predetermined dielectric function of the alloy thin films, the SPP dispersion–relation can be directly computed (see Figure 3g lower row). An excellent agreement with the experiment is observed, both of which demonstrate unambiguously the progressive transition of the dispersion curve from pure Ag to pure Au and the well-controlled optical behavior with the variation of the Au:Ag ratio.

In principle, the permittivity of polyelemental metallic mixtures can be tailored to match a desired optical response, which could be used in the inverse design of photonic devices. Nevertheless, in these cases the experimental determination of ε could involve the fabrication of a very extensive number of samples through a trial-and-error conventional approach. Instead, one could use machine learning (ML) to predict ε for metallic mixtures ranging from binary to multicomponent ones, including the effects of small chemical composition variations. In Section 6, we provide our vision for how ML could accelerate the design of optical materials with *on demand* optical behavior.

3.2.3. Electronic Band Structure

Quantum mechanically, the interband and intraband transition probabilities are determined by the electronic band structure of the alloy system. Therefore, incorporating the electronic band structure into ε is needed for a more accurate description of the optical response of a metal. Inspired by the critical point

analysis of the metal band structure,^[82] a parametric analysis model for ε in an alloy system has been proposed by Rioux et al.,^[54] which suggests that the most important features in ε are largely determined by the critical points (Van Hove singularities) in the joint density of states (jDOS). The Lorentzian term $\varepsilon_{\text{ib}}(\omega)$ in the dielectric function can be transformed to include the jDOS term as

$$\varepsilon_{\text{ib}}(\omega) = A \int_0^{\infty} \frac{\text{jDOS}(\omega_k)}{\omega_k (\omega_k^2 - (\omega + i\gamma)^2)} d\omega_k \quad (2)$$

where l and k are the occupied and empty electronic states, respectively, and A is the oscillator amplitude encompassing the transition matrix element given by Fermi's golden rule. As jDOS is mainly influenced by the critical points in the band structure, considering the transitions near the X and Γ points is adequate. By assuming a parabolic jDOS profile around these points, the parametric analysis model includes a total of 30 fitting parameters to fully describe the frequency-dependent ε for Ag–Au, and can be generalized to other alloy systems as well.^[40,43] This approach relies on the known band structures of pure Au and Ag with different fitting parameters, followed by a weighted summation of ε_{ib} of the two metals.

In the past, there have been various reports on the direct calculation of the band structure of alloys using density functional theory (DFT).^[52,65] As a very recent example, Krayer et al.^[68] have shown explicitly how each metal contributes to the overall band structure of the Ag–Au alloys. As presented in Figure 3h, Au dominates most of the high-energy states in the alloy's d-band, whereas comparable contributions from Au and Ag are observed for other states across all critical points of the Brillouin zone. In another work by McClure et al. on Au–Pd,^[83] the addition of Pd results in strong hybridization close to the Fermi level, with Pd dominating the values and profiles of the additional d-bands. Overall, we envision that the DFT-based alloy's band structure calculation and the parametric analysis method could be combined to precisely and efficiently model ε in alloys.

4. Applications

Benefiting from the combination of the optical properties of one or more metal elements with the catalytic, thermal, chemical, or magnetic properties of others, various alloy-based photonic devices have flourished over recent years. This section is intended to present the advances on the employment of alloy-based structures and devices in a wide range of territories spanning from superabsorbers to renewable energy systems.

4.1. Thin Film Superabsorbers

Superabsorbers are artificial optical materials/structures presenting a near-unity light absorption over a broad or selected narrow band of the electromagnetic spectrum. Typically, the ultrahigh absorption arises from impedance matching between the surrounding medium and the material.^[84] One approach to achieve this requirement in the visible to NIR wavelength range

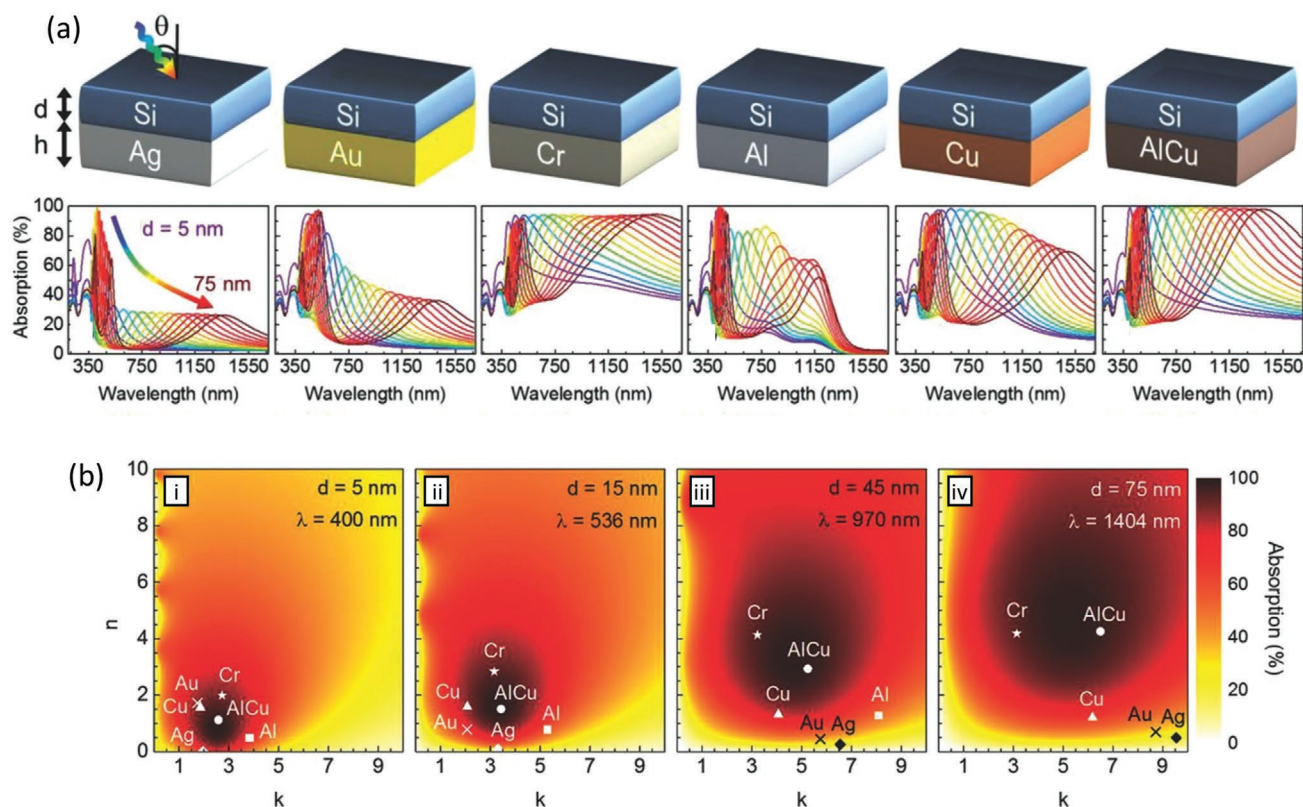


Figure 4. Metal alloys for superabsorbers. a) Upper row: schematic of the bilayer semiconductor/metal thin film superabsorbers. Lower row: calculated absorption spectrum of each device with varying thickness d of the Si layer. b) Comparison of the absorption maps with respect to the material's refractive index for different wavelengths and Si layer thicknesses d . The AlCu alloy outperforms its pure metal counterparts as well as Au, Ag, and Cr. Adapted with permission.^[19] Copyright 2018, Wiley.

of the electromagnetic spectrum is to utilize an ultrathin planar film as the absorber unit cell.^[85] The optical losses in this thin film give rise to nontrivial interference, which results in strong absorption. The absorber active layer contains a semiconductor thin film (e.g., Si or GaAs) on top of a metal substrate. The active layer is required to possess high values of ϵ_2 in the frequency range of interest to achieve ultrahigh absorption.^[69]

To realize adjustable optical absorption in this thin-film structure, a superabsorber device employing AlCu as the metal substrate has been reported in a recent work from our group.^[19] Here, the unit cell is a bilayer structure where an ultrathin Si slab sits on top of the AlCu thin film. In this device configuration, above and subbandgap photons are mostly absorbed by Si and by the metallic thin-film layer, respectively. As shown in **Figure 4a**, the device outperforms those composed of pure metal substrates, reaching near-unity absorption (>99%). In addition, the structure supports dual-band absorption. Further, the resonance can be fine-tuned by varying the thickness of the semiconductor layer, spanning the entire UV–vis–NIR range of the spectrum. At the same time, the shift of the absorption peak does not attenuate its intensity, as opposed to other pure-metal-based devices. This remarkable performance is attributed to the change of the dielectric function as mentioned in prior sections: the low magnitude of ϵ_1 over the entire spectrum combined with the large ϵ_2 particularly in the NIR regime. The n – k contour maps in **Figure 4b** show that the AlCu alloy-based cell

always outperforms the other candidate materials provided the thickness of the Si layer is greater than 15 nm. Further, even under oblique incidence up to 50°, the main resonance mode still absorbs 95% of incident light for unpolarized incidence, a manifestation of the device being a super absorber with great tolerance to polarization and incidence angle change. This scalable approach has the advantages of being composed by metals that are CMOS compatible and earth-abundant. It is likely that other metal combinations, not yet explored, could perform equally well to the example provided here.

4.2. Hot Carrier Devices

Light absorbing metal films and nanostructures can also be used for novel optoelectronic devices that exploit hot charge carrier effects. When light is coupled into a surface plasmon mode, there are two decay routes for the plasmon: radiative decay into photons and nonradiatively into energetic charge carriers with excessive kinetic energies, i.e., hot carriers.^[7] These hot carriers can drive chemical reactions directly, or be collected as photocurrent across a metal–semiconductor Schottky junction or a metal–insulator–metal junction, before losing their energy through electron–electron and electron–phonon interactions, typically on a timescale of 100 fs–1 ps.^[86] While hot carrier effect in metals have found numerous applications, ranging from

photocatalysis to photosensing and photovoltaics,^[27,87,88] most work has been limited to pure metals. Hence, metal alloys present a new opportunity to tune and control hot carrier effects for improved devices and new applications.

The initial energy distribution of hot carriers upon excitation plays a critical role in the efficiency of the subsequent injection into the junction, as it determines the fraction of the carriers that have enough energy to traverse the junction barrier and be collected by the counter electrode. This distribution depends on the electron density of states (EDOS) of the metal, which is fixed for a specific pure metal, and incident illumination. Gong and Munday^[89] have adopted an effective, yet simple, EDOS calculation to derive the energy distribution in different alloys, which results in configurations not attainable with pure metals (see Figure 5a). Depending upon the incident photon energy and the EDOS, hot carriers end up with different energy profiles. For example, both Ag and Cu have relatively flat distributions

when illuminated with near-IR light; however, their alloy shows sharp features in the distribution of both electrons and holes, which is advantageous. Similarly, alloys of other metals can produce a variety of distributions that differ significantly from their pure metal counterparts. Alloying can also be used to increase light absorption within the metal, while still maintaining long carrier attenuation lengths, as shown by Krayer et al. with Ag–Au alloys.^[68] With known hot carrier energy profiles, one can choose proper doping types and concentrations in the semiconductors to form Schottky junctions with adequate barrier height for efficient current generation.

In addition to having an appropriate energy distribution, the carriers must have a lifetime that is long enough to make it to the metal–semiconductor junction without relaxing and losing energy. The electron–phonon interactions, which usually result in the electrons losing energy to the lattice, vary from material to material. Thus, metal alloys offer an opportunity to

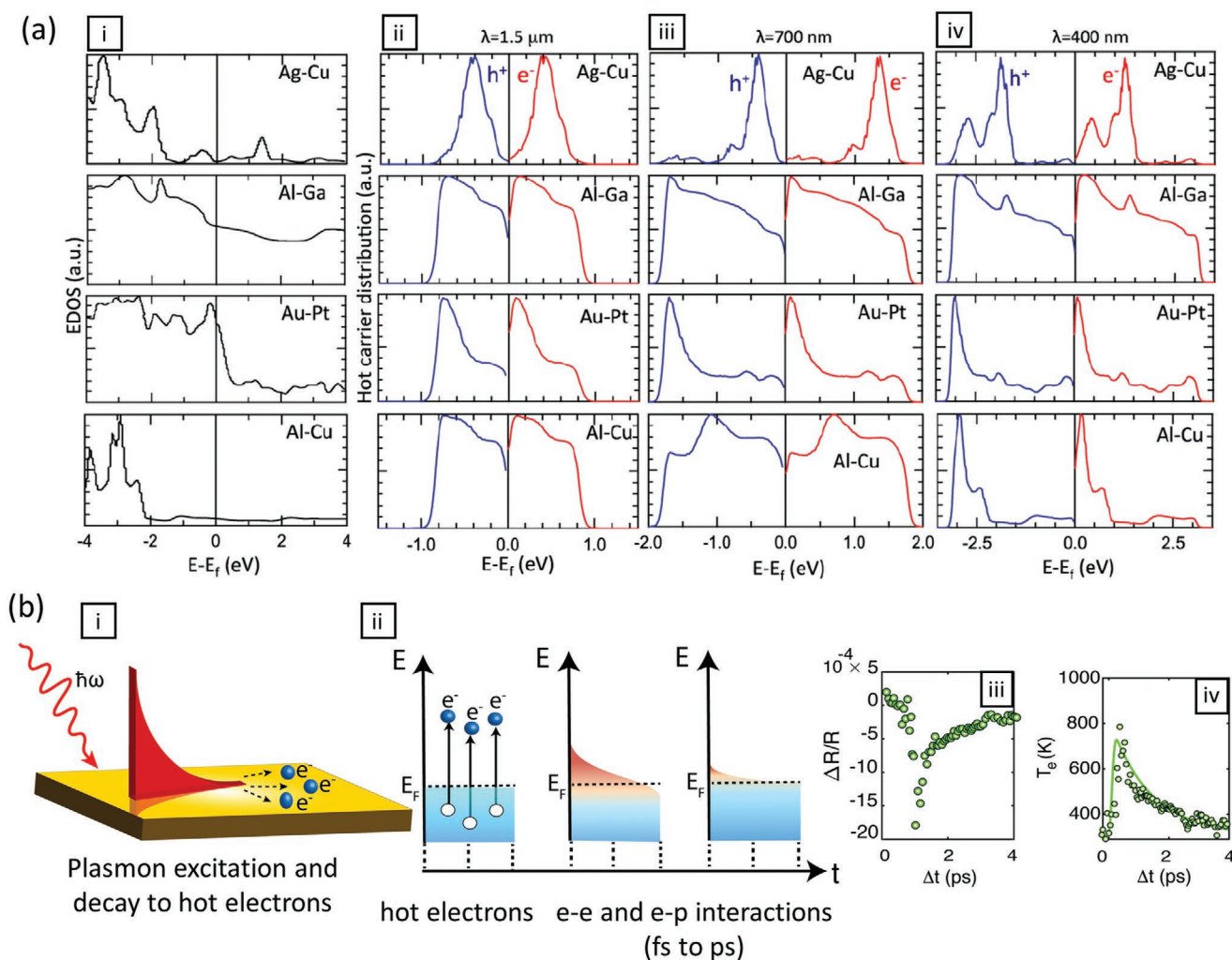


Figure 5. Metal alloys for hot carrier devices. a) Hot carrier initial energy distribution upon excitation by various photon energies in different alloys. Adapted with permission.^[89] Copyright 2015, Optical Society of America. b) (i) Schematic of the excitation of the hot electrons in a thin gold film after coupling to the propagating surface plasmon. (ii) Pump pulse excites the electrons to energy states above the Fermi level, leading to an increase in the electron's temperature. The hot electrons eventually cool down and dissipate their energy to the lattice following a series of electron–phonon coupling processes. (iii) Differential reflectivity measurement at resonance wavelength and (iv) electrons temperature distribution as a function of delay time between pump and probe pulses. Adapted with permission.^[90] Copyright 2020, Optical Society of America.

tailor and potentially suppress these interactions. To measure the relaxation time, ultrafast pump-probe measurements are typically employed in which a high-power pump beam induces changes in the transmission or reflectivity of the sample (see Figure 5b). These changes are then monitored with a lower power probe beam, and data can be used to determine an effective carrier temperature, which reduces over time as energy is released into the lattice. Laser fluence and electric field confinement caused by the surface plasmon resonance are external factors that can modify the hot-electrons relaxation dynamics.^[90] It has also been shown that sample geometry and the material's band structure affect the relaxation time of the hot electrons.^[91] These results suggest that the complex interplay between the atoms and the electrons in alloyed metals presents an additional route for tuning of hot carrier dynamics. As an example, we recently showed that the addition of 2% Ag into Au can increase carrier lifetime by $\approx 35\%$.^[92]

4.3. Optical Hydrogen Sensors

H₂ gas is an ideal clean energy source candidate because when burned, it emits no greenhouse gases and can be easily transported to regions where high voltage power lines cannot reach. With the increase in H₂ usage, high-quality sensors are needed to regulate the flammability risks. In particular, optical H₂ sensors are ideal due to a decreased risk of sparking in a flammable H₂ environment when compared to electrical ones. These optical sensors utilize the change in a material's optical properties as it hydrogenates, either through a shift in a nanoparticle's LSPR resonance or a change in the reflectance from a metallic thin film. Traditional H₂ sensors are based off pure Pd because of its ability to absorb and desorb H₂ at room temperature depending on the gas partial pressure. However, there are multiple issues with Pd-based H₂ sensors including a high intracycle hysteresis, a limited pressure measurement range, a slow response time, and being easily poisoned by gases found in the atmosphere, such as CO and NO₂.^[93] Recently, alloying Pd with other metals has created the opportunity to greatly decrease or eliminate these negative characteristics, while maintaining a high sensing quality.^[4,22,93–97]

Au is the most common material alloyed with Pd to improve its ability to function as a commercial sensor.^[4,93–96] By alloying these two metals the initial dielectric function of the metallic mixture can be tuned as well as the metal's response to H₂ exposure.^[94] The main benefit of Pd–Au is that it eliminates the sensor hysteresis.^[93,95,96] This feature is a deleterious characteristic in a sensor, because it causes an ambiguity of H₂ pressure depending on whether the sensor is on the loading or unloading portion of the cycle. The hysteresis in Pd sensors stems from the α to β phase transition of the hydrogen in the metal lattice, which results from its retention during unloading. Alloying Pd with Au suppresses this phase transition by lowering the critical temperature of the α – β miscibility gap, causing the elimination of the hysteresis and allowing for a one-to-one readout of the sensor.^[93,95,96] This suppression of the phase transition in Pd–Au also has the added benefits of increasing the detectability range and decreasing the response time of the sensor.

Pd–Cu is another alloy commonly used for hydrogen sensing, due to the addition of Cu to the Pd lattice introducing a high resistance to sensor poisoning.^[22,97] This combination allows the sensor to work in atmospheric conditions, eliminating degradation when exposed to gases such as CO.^[22] Furthermore, sensing with Pd alloys has been improved by moving to ternary systems, where the benefits from multiple metallic elements are combined into a single material. As an example, the addition of both Au and Cu to Pd has led to a H₂ sensor that combines the chemical resistance of Pd–Cu alloys with the improved sensing performance of Pd–Au alloys, as shown in **Figure 6b**, creating a hysteresis-free sensor that is proven resistant to CO exposure.^[22]

In addition to Pd, Mg is another material with favorable sensing qualities. Although pure Mg cannot absorb H₂ at standard temperature and pressure, if this metal is capped with a thin (≈ 3 nm) layer of Pd, then it readily absorbs H₂.^[98] Mg has a much larger change in optical properties than Pd and has a much lower weight to hydrogen ratio, making it important for H₂ storage. By alloying Mg with other metals, such as Ti, Ni, or Ca, switchable devices can be made that have a high reflection when under ambient atmosphere (metallic state) and have a high transmissivity in the visible spectrum when under H₂ gas (hydride state). An example of this extreme tunability can be seen in Figure 6c, which depicts the reflection and transmission spectra of a Mg_{0.94}Ca_{0.06} alloy, where the transmission increases from near zero in the metallic state to $\approx 45\%$ in visible spectrum in the hydride state.^[99] This tunability is relevant for applications such as coatings for solar collectors or smart windows, switchable mirrors, and tunable reflectors.^[99–102]

4.4. Plasmon-Enhanced Catalysis

Plasmon-enhanced catalytic effects utilizing metallic films and nanostructures have been a main focus of research by chemists and materials scientists, and widely explored in the past.^[103–105] The employment of alloyed nanostructures in similar applications has thus emerged to further improve upon the initial results with pure metals. This section provides an overview of how different alloy nanostructures have been utilized in various plasmon-enhanced catalytic systems.

A photoelectrochemical water-splitting cell consists mainly of a metal–oxide–semiconductor photoanode (e.g., TiO₂), where photocarriers are generated and extracted to drive the oxygen and hydrogen evolution reactions on the semiconductor surface and the metal counter electrode.^[106] The metal–oxide–semiconductor layer does not absorb visible light well due to its large bandgap energy. Thus, metal nanoparticles are usually decorated on top of the photoanode to boost visible light absorption and excite hot electrons. These hot electrons are subsequently injected into the semiconductor layer and extracted to foster corresponding chemical reactions.

In photoelectrochemical cells, the plasmon-induced hot electron energy profile primarily determines its performance. For this reason, Au nanoparticles are not an ideal option for the cell because of its relatively low interband transition energy (≈ 2.3 eV), which results in the generation of hot electrons with low energies. By contrast, Ag can excite higher energy hot electrons due to intraband transitions. As shown in Section 3.1,

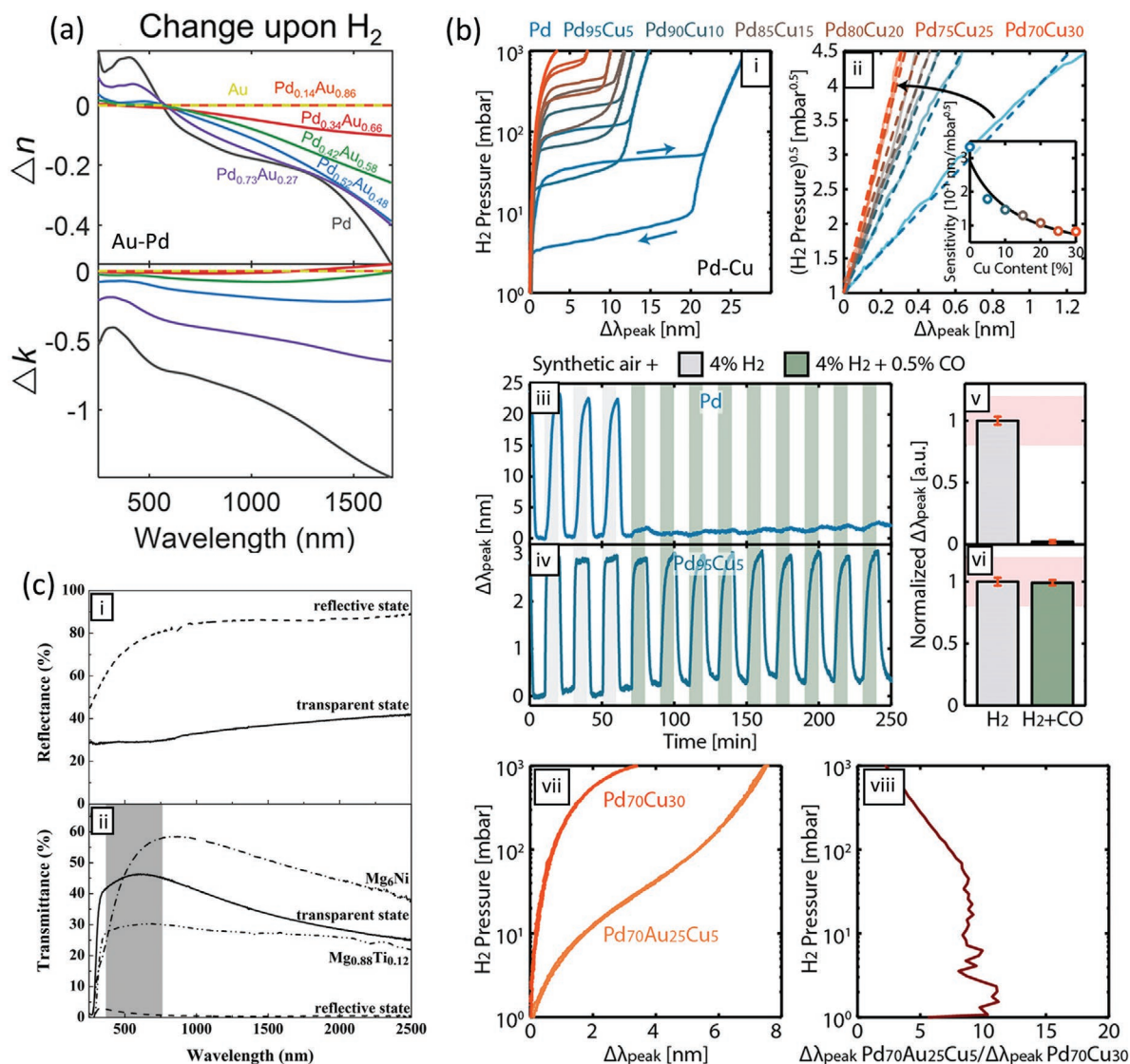
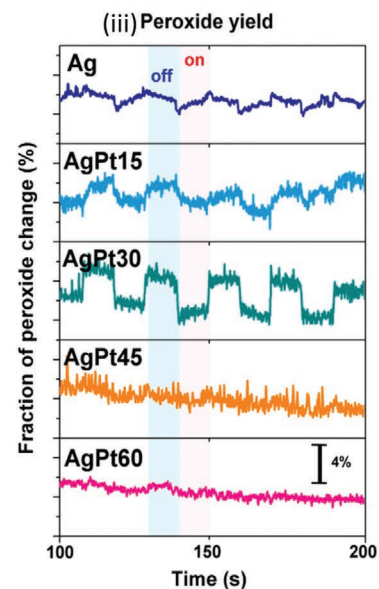
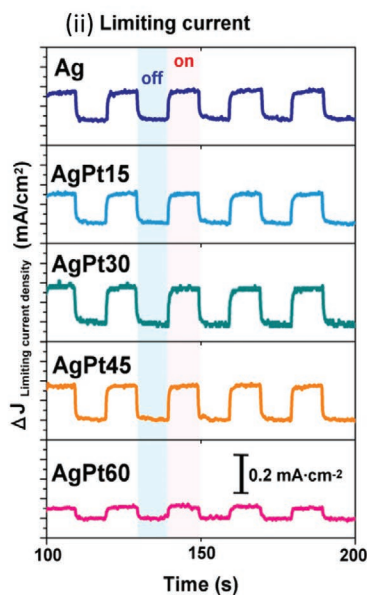
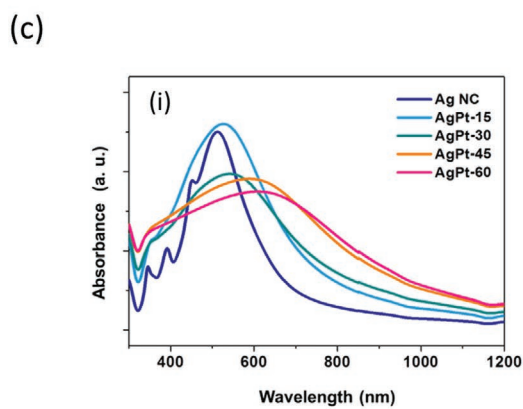
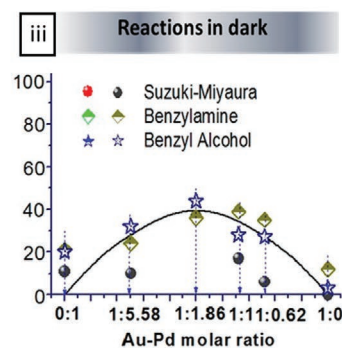
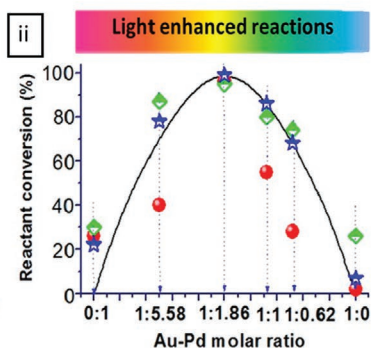
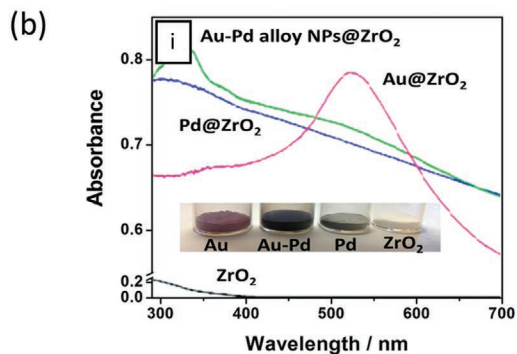
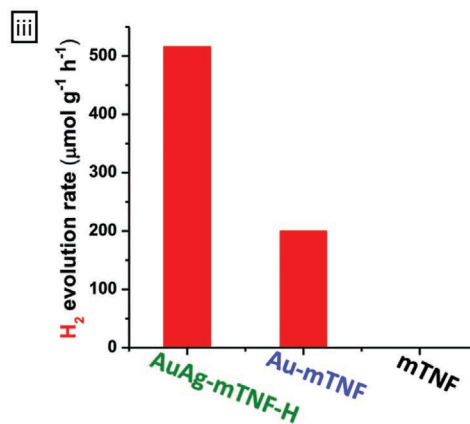
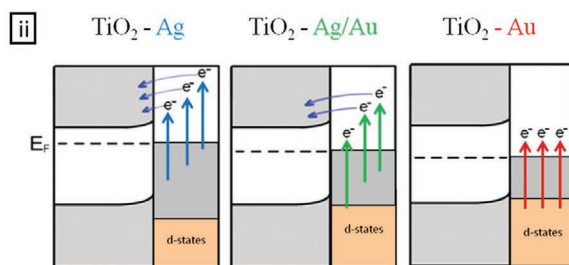
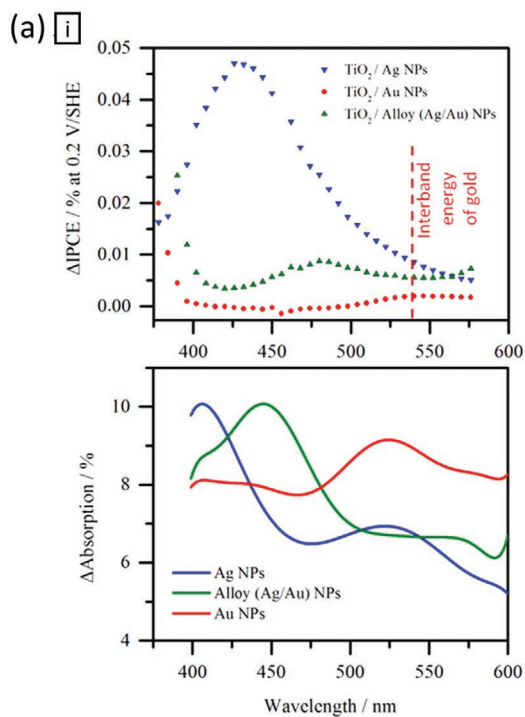


Figure 6. Metal alloys for hydrogen sensors. Clockwise: a) change in the refractive index ($n-k$) upon hydrogenation of different Pd_xAu_{1-x} alloys. Adapted with permission.^[94] Copyright 2019, American Chemical Society. b) Hydrogen sensor measurements of Pd-Cu and Pd-Cu-Au alloys. (i,ii) Optical isotherms of the Pd-Cu. (iii-vi) Comparison of resonance peak change during cycling of Pd versus Pd₉₅Cu₅, showing that the addition of Cu to Pd increases chemical poisoning resistance, but decreases signal. (vii) Optical absorption and desorption isotherm of Pd₇₀Cu₃₀ and Pd₇₀Au₂₅Cu₅ and (viii) sensitivity enhancement due to the addition of Au. Adapted with permission.^[22] Copyright 2019, American Chemical Society. c) (i) Reflectance and (ii) transmittance data for a Mg_{0.94}Ca_{0.06} switchable mirror. Transmittance data is compared with Mg_{0.88}Ti_{0.12} and M₆Ni switchable mirrors. Adapted with permission.^[99] Copyright 2009, AIP Publishing LLC.

alloying Ag with Au can redshift the resonance wavelengths while retaining relatively high energies for excited hot electrons. Valenti et al.^[107] have recently demonstrated that a photoelectrochemical cell using Ag-Au nanostructures can significantly alter the hot electron energy profile as a result of both the optical resonance shift and the alteration of the material's EDOS, hence the peak response shift of the incident photon conversion efficiency (IPCE) (see Figure 7a(i)). The alloy displays a progressively increasing EDOS in the d-band around 3 eV below the Fermi energy, which increases the probability of intraband transitions between 450 and 520 nm in the visible light spectrum range (see Figure 7a(ii)). It is noted that the cocatalytic property of the alloy nanoparticles that facilitates

charge transfer from the semiconductor surface to the electrolyte may also play a prominent role in enhancing the incident photon to current efficiency. To achieve further improvement, a trade-off between the plasmon absorption peak shift and favorable hot electron energy profile ought to be carefully considered.

A similar Ag-Au alloy-TiO₂ based photoelectrochemical system has been reported by Chattopadhyay et al.^[108] In lieu of a bulk TiO₂ photoanode layer, a layer of mesoporous TiO₂ nanofibers (mTNFs) is fabricated by a specifically designed electrospinning synthesis protocol. The Ag-Au nanoparticles are anchored on the surface of the mTNF layer. Under simulated solar illumination (60 mW cm⁻²), both the alloy and the mTNF



layers absorb solar light and drive the H₂ evolution at a rate as high as 516 μmol h⁻¹ g⁻¹, more than 2.5 times faster than using pure Au nanoparticle-decorated cell (see Figure 7a(iii)).

Pd is a well-known active catalyst for many organic synthesis reactions. In many of these reactions, heating is required to improve the yield and efficiency, which is energy-intensive.^[109] Further, recovering the homogeneous Pd catalyst postreaction for reuse is challenging. An alternative option is metallic nanostructures such as Au and Ag, which have found extensive applications in photocatalysis due to their strong LSPR coupling that creates high energy conducting electrons at the metal surfaces, promoting the activation of molecules for chemical reactions at the surface.^[110]

To integrate the catalytic effect and the strong plasmonic effect of noble metals, Sarina et al.^[111] blend Pd and Au to form alloy nanoparticles as catalysts for more efficient organic synthesis. The resulted charge heterogeneity at the alloy particle surface facilitates the interaction between the particles and reactant molecules compared with that at the surface of pure Pd. Furthermore, under irradiation the LSPR-excited electrons with high energies collected at the Pd site further strengthen the catalytic activity at ambient temperature while the electrons remain in the “hot” state. The alloy nanoparticles are fabricated by impregnation–reduction method, with an average size of 3–6 nm, and the plasmonic absorption peak is observed in the near-UV regime (see Figure 7b(i)). For three particular types of reactions, the impact of alloying on the dark and light yield varies tremendously (see Figure 7b(ii),(iii)). For instance, under optimal conditions (Au:Pd molar ratio, irradiation wavelength range and intensity), the irradiation increases the product yield of Suzuki–Miyaura cross coupling to 96% from 37% in the dark, much higher than the yield (26%) with pure Pd and that (2%) with pure Au under irradiation. The irradiation-induced yield of the selective oxidation of aromatic alcohols reaches 100%, much higher than 22% with pure Pd, and 7% with pure Au. Interestingly, the Au:Pd ratio of 1:1.86 is found to be the optimal value for all aforementioned reactions due to the favorable charge distribution in the excited state upon LSPR resonant absorption (see Figure 7b(ii),(iii)). This alloy-based photocatalyst opens the door for achieving a wide range of efficient organic synthesis reactions. Other recent works reported various alloy combinations (Au–Pd, Au–Cu, Ag–Pd) and their resulted yield improvement of various categories of organic synthesis reactions (cross-coupling, benzyl alcohol oxidation, nitrobenzene reductive coupling, nitrophenol reduction).^[112–116]

Efficient oxygen reduction reaction (ORR) is crucial for developing electrochemical systems such as metal–air batteries and fuel cells. The activity of ORR is closely correlated to the surface nature (e.g., element and crystalline facets) of the catalysts.^[117]

In addition, during ORR hydrogen peroxide can be generated as an intermediate product due to an undesired side reaction and can reduce its overall yield. Thus, there is a critical need for suppressing this intermediate product. In a recent work by Lin et al.,^[118] an edgeless Ag–Pt alloy nanocage-shaped catalyst is implemented to minimize the production of hydrogen peroxide, and to increase the current generation through plasmonic effects. As Figure 7c(i) shows, by increasing Pt content, the LSPR resonance peak redshifts from 526 nm for pure Ag to 645 nm for Ag–Pt alloy with 23% Pt content, while continuously broadening. The increase of limiting current density in the amperometric measurement is indicative of the plasmonic absorption and the plasmon-induced heating (see Figure 7c(ii)). Figure 7c(iii) demonstrates that the illumination on the Ag–Pt alloy nanocages suppresses the formation of hydrogen peroxide. Interestingly, the transfer of hot electrons after plasmonic absorption plays a pivotal role in suppressing the intermediate formation as the vacancies in the 5d state of Pt are altered. Further, the enhanced LSPR field facilitates the rapid migration of reactants at the nanocage surfaces, further reducing the peroxide yield. Analogously, Li et al.^[119] has implemented a composite catalyst architecture formed by a 3D mesoporous graphene network with ultrafine Ag–Pt alloy nanoparticles (≈2.5 nm in size) dispersed on the surface, exhibiting 3.5× higher mass catalytic activity for ORR, compared with a commercial Pt/C (TKK) catalyst.

4.5. Photovoltaics

Considering the extensive number of reports in the literature describing the benefits of using metallic nanostructures to increase the overall power conversion efficiency of solar cells, we limit this section to a brief discussion of how alloys with *on demand* permittivity could be exploited for specific types of photovoltaic devices. Shortly, the primary mechanisms responsible for the efficiency enhancement widely reported in the literature thus far are: optical path length increase, scattering-induced waveguide mode coupling, and boosted field intensity caused by plasmon resonances. All of these processes help to increase the light absorption in the active layer of the solar cell, hence improving the overall performance of photovoltaic devices. Au, Ag, Cu, and Al are the most commonly used metals in plasmonic solar cells, and they each are suitable for different resonance wavelength ranges, determined by their dielectric functions and the size and shape of the nanostructure. As discussed earlier, alloying allows for the customization of ϵ , which then alters the resulting plasmonic responses and solar light absorption.

Although the efficiency of perovskite solar cells has soared since its discovery,^[120] further performance improvement using

Figure 7. Metal alloys for photocatalysis. a) Photoelectrochemical water-splitting. (i) Absorption spectra, and the change of IPCE in Au–Ag-incorporated photoelectrochemical cell compared with pure metals. (ii) Hot electron energy profile due to plasmonic absorption, in Au, Ag, and Au–Ag. Adapted with permission (direct link: <https://pubs.acs.org/doi/full/10.1021/acsp Photonics.6b01048>).^[107] Copyright 2017, American Chemical Society (Note: further permissions related to the material excerpted should be directed to the ACS). (iii) H₂ evolution rate in Au–Ag–mTNF, compared with Au–mTNF and bare mTNF. Adapted with permission.^[108] Copyright 2019, American Chemical Society. b) Au–Pd nanoparticle catalysts for organic synthesis reactions. (i) Absorption spectra of samples with Au–Pd alloy, Au, and Pd nanoparticles, and the control. Inset: photograph of fabricated samples. (ii) Reaction conversion rate of three particular types of organic synthesis (ii) under irradiation and (iii) in the dark. Adapted with permission.^[111] Copyright 2013, American Chemical Society. c) Light-induced oxygen reduction reaction (ORR). (i) Absorption spectra of alloyed nanostructures. (ii) Limiting current density enhancement and (iv) suppression of peroxide intermediate product. Adapted with permission.^[118] Copyright 2017, American Chemical Society.

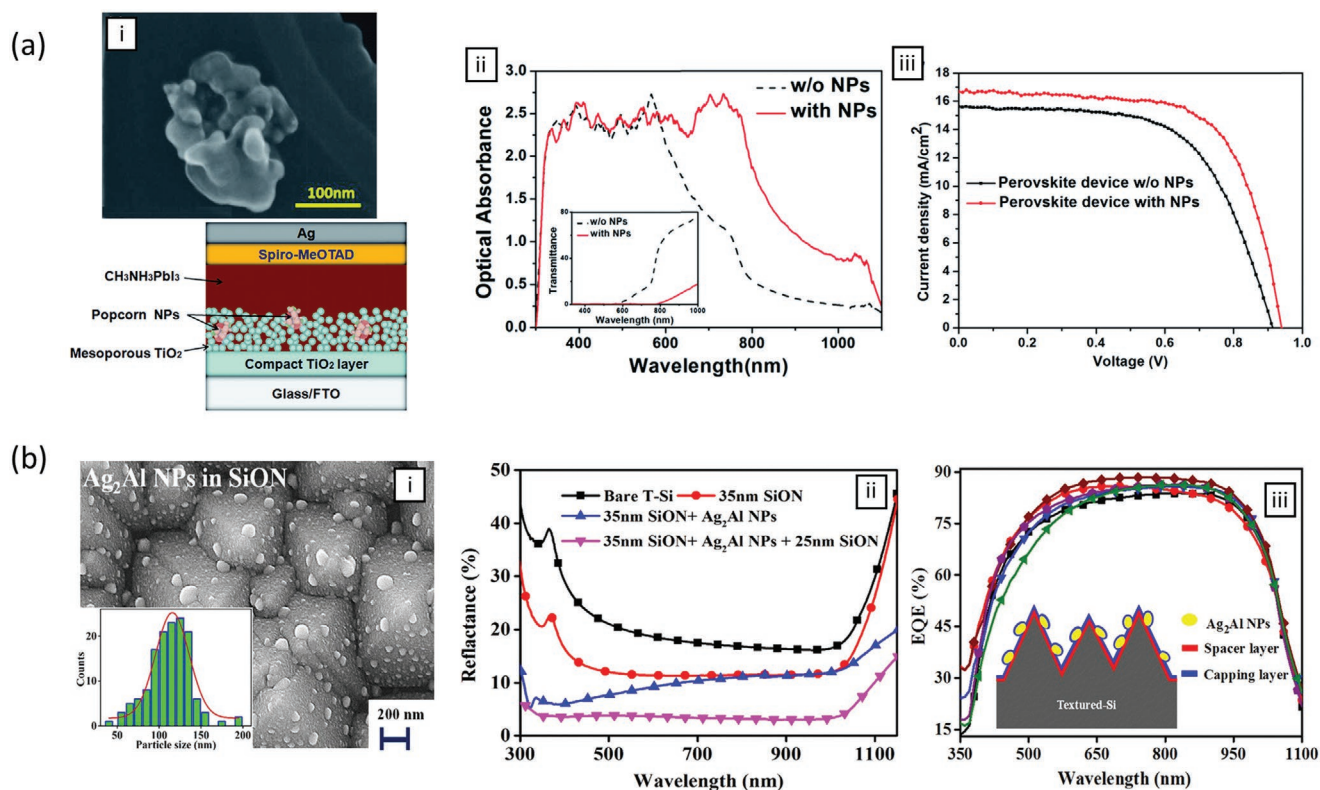


Figure 8. Metal alloys for plasmonic solar cells. a) (i) Schematic of perovskite solar cell with irregular shaped Au–Ag nanoparticles embedded in a TiO_2 layer. (ii) Optical absorption and (iii) J – V characteristic with and without the alloyed nanostructures. Adapted with permission.^[122] Copyright 2015, Royal Society of Chemistry. b) (i) SEM image of Ag–Al nanoparticles sprinkled in the SiON matrix. Inset: size distribution of the particles. (ii) Reflectance spectra and (iii) EQE for: bare Si solar cell, devices with SiON matrix, with nanoparticles on SiON matrix, and with nanoparticles on SiON matrix capped by SiON layer. Adapted with permission.^[127] Copyright 2017, Nature Publishing Group.

plasmonic nanostructures had been scanty.^[121] An Ag–Au alloy-based plasmonic $\text{CH}_3\text{NH}_3\text{PbI}_3$ device has recently been reported by Lu et al.^[122] The alloyed nanoparticles utilized in this work are fabricated by a coreduction synthesis method, and are embedded in the mesoporous TiO_2 layer (see Figure 8a(i)). Each particle adopts an irregular shape, with different fine geometrical structures and varying Ag:Au molar ratios at different locations of the particle. As a result, various LSPR modes of distinct frequencies, polarizations, and field patterns can be supported. Due to the tailored dielectric function and the fine structures, the Ag–Au nanoparticles dramatically boost the light absorption in the broadband NIR wavelength range of the spectrum, especially around the band edge of the material (720–820 nm), and improve the charge carrier transfer rate (see Figure 8a(ii)). This results in an overall increase in efficiency from 8.9% to 10.3% (see Figure 8a(iii)).

In dye-sensitized solar cells, the photoanode material is usually required to absorb 80% of light over a very broad range of solar spectrum for acceptable power conversion efficiency; however, high absorption is difficult because the active region of these devices is typically small due to poor charge separation and transport.^[123] To increase the optical absorption over a broad frequency range, Xu et al.^[124] have implemented a similar device configuration decorated with plasmonic Ag–Au alloyed nanostructures. The power conversion efficiency of the solar cell decorated with 2.38 wt% of Ag–Au nanoparticles reaches

6.09%, corresponding to a 16% enhancement compared with the bare TiO_2 -based device. Further improvement can be realized by adding an opaque diffusive back reflective layer at the counter electrode so the backward scattered light excites LSPR modes at more “hot spots” on the back side of the alloy nanoparticles. Then, the performance is found to be elevated to 7.85%, corresponding to a 32% enhancement for this case.

As for traditional Si-based plasmonic solar cells, a commonly used metal is Ag because of its favorable dielectric function.^[125,126] Yet, Ag-based nanostructures are generally subject to parasitic absorption loss and poor surface adhesion on semiconductor substrates. To overcome this issue, Parashar and Komarala^[127] have reported a Si solar cell that incorporates Ag–Al alloy nanostructures. As expected, ϵ_2 for Ag–Al changes significantly from that of pure Ag due to the shift of the interband transitions at the L points as Al replaces Ag in the lattice, while the real part only displays minimal changes in the visible wavelength regime. In turn, this feature helps reducing parasitic light absorption. In this solar cell device, the nanoparticles are embedded in dielectric SiON matrix (see Figure 8b(i)), which consists of a spacer and a capping layer. The spacer layer lowers the refractive index gradient between Si and air. The capping layer that covers the Ag–Al alloy reduces the phase mismatch between the incident and scattered light fields, further improving the forward scattering. As a result, the optical reflectance is reduced substantially, leading to a large absorption over

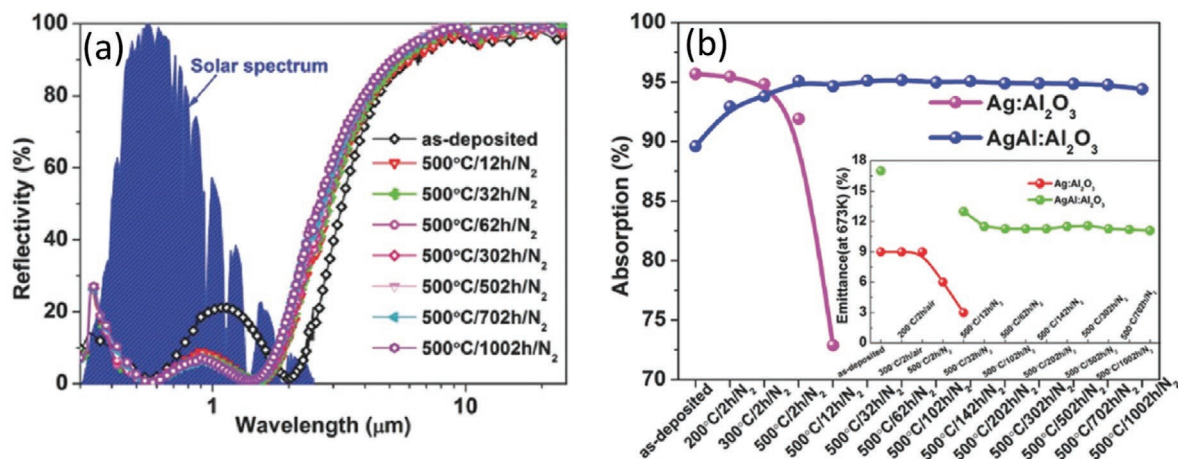


Figure 9. Metal alloys for solar thermal absorbers. a) Reflectivity spectra of the multilayer nanocermet structure compared with solar spectrum under different annealing conditions. b) Solar absorbance and thermal emittance (inset) comparison between Ag–Al alloy-based nanocermet and pure Ag-based nanocermet. It is evident that the former has much stronger absorption and emission at high temperature. Adapted with permission.^[129] Copyright 2016, Wiley.

a broad wavelength range and a considerable carrier generation improvement in the underlying Si layer. The device with the 35 nm Ag–Al nanoparticle/25 nm SiON exhibits a minimum average reflectance of $\approx 3.6\%$ in the 300 nm to 1.15 μm wavelength range (see Figure 8b(ii)) and, as desired, a large external quantum efficiency (EQE)—close to 85% for 600–900 nm (see Figure 8b(iii)). The same structure thus presents a strong increase in both the short-circuit current J_{SC} (34.61 mA cm^{-2}) and the overall power conversion efficiency (15.04%) compared with the bare textured Si-based device (26.27 mA cm^{-2} and 10.82%, respectively).

4.6. Solar Thermal Absorbers

Solar thermal absorption is an alternative way to harvest solar energy in the form of heat. Similar to photovoltaic applications, Ag-based nanostructures are among the most common metal nanostructures employed in plasmonic solar absorbers. However, its relatively low melting point ($\approx 960^\circ\text{C}$) poses a challenge for reliable high-temperature plasmonic behavior because of thermal-induced aggregation or sublimation.^[128] Therefore, alloying Ag with a thermally tolerant metal would help to improve the thermal stability and furthermore enable controllable plasmonic behavior that meets the solar selectivity.

To demonstrate this concept, Gao et al.^[129] have reported a solar absorber device composed of Ag–Al alloy nanostructures mixed with Al₂O₃ matrix, which forms a nanocermet composite. This nanocermet is comprised of highly dispersive Ag–Al nanoparticles scattered in the Al₂O₃ matrix. Here, the Al-dopant level determines the thermal and structural stability, as well as the plasmonic behavior of the nanocermet. The absorption spectra in the range of 300 nm–2.5 μm exhibit pronounced LSPR peaks and relatively broadband absorption profiles, yet optical degradation arises as the annealing time and temperature are increased for pure Ag-based cermet, but not for Ag–Al ones. This thermal stability is attributed to the formation of an alumina capping layer on the Ag–Al nanoparticles during

annealing. Ultralow reflectance within the entire solar spectrum is observed in the structure (see Figure 9a), even under thermal annealing at 500 °C for a significantly long duration (up to 1002 h). The effective solar absorbance for this device is as high as 95% with excellent thermal stability. Moreover, the effective thermal emission is also considerably enhanced compared with pure Ag-based nanocermet (see Figure 9b). The improved optical performance and thermal stability of the Ag–Al alloy nanocermet demonstrate great promise of alloy nanostructure-based solar thermal applications.

5. Summary

In conclusion, metal alloys offer tremendous opportunities in shifting the paradigm from pure metal-dominant plasmonics and photonics due to their customizable optical properties, not attainable with pure metals. Their permittivity can be readily controlled by tailoring their chemical composition, an underexplored and powerful variable. To date, several fabrication methods have been successfully implemented to achieve metal alloyed subwavelength nanostructures, ranging from co-sputtering followed by thermal annealing, sequential pulsed laser deposition, scanning probe block copolymer lithography, and conventional lithography-based routes. The main next challenge regarding fabrication is the development of a high-precision and low-cost method for large-scale applications.

Concerning nanoscale alloys' optical response, a primary figure-of-merit that can be tailored using chemical composition is the optical extinction spectra. Its peak wavelength and intensity have been shown to vary significantly in binary and ternary metallic mixtures, which is critical for applications ranging from superabsorbers to photovoltaics. The accurate determination of the permittivity of metal alloys has relied on variable-angle spectroscopic ellipsometry measurements and its modeling. Here, most material characterization has focused on demonstrating how both ϵ_1 and ϵ_2 in alloys vary nonmonotonically in comparison to its pure counterparts. In turn, this

feature can enable access to values of ϵ difficult to achieve with pure metals.

Metal alloys have demonstrated superior performance over pure metals in superabsorbers, hot carrier devices, hydrogen sensors, photocatalytic systems, photovoltaics, and thermal solar absorbers, among other devices. As stated earlier, usually the alloying process is a pathway for obtaining a metallic material with tailored values of ϵ . In some cases, by alloying two or more metals one can benefit from the optical properties of one and the mechanical, chemical or thermal properties of the other(s), resulting in a composite. Thus, metal alloys are a versatile material system that has been under-utilized until recent years, which are leading to a number of new photonic devices and applications for next-generation optoelectronics.

6. Outlook

From a material's perspective, while alloys of coinage and noble metals such as Au, Ag, Cu, Pt, and Pd have been most heavily utilized, challenges remain including relatively high cost, bioincompatibility, etc. Thus, earth abundant metals such as Al, Mg, and Ca are promising alternatives for creating metallic mixtures for photonics. To date, the research in Al and Mg has been primarily focused on its mechanical and thermal properties for aerospace applications. Yet, its CMOS-compatibility and the low values of ϵ_2 in the UV–vis range of the spectrum, are unique attributes that should not be neglected when designing metallic mixtures.

Bimetallic alloys have been the mainstream basis in alloy-based structures and devices. Yet, more degrees of freedom in controlling the optical properties can be provided by alloying three or more metals. This can ideally provide more abundant choices for ϵ based on needs and associated applications. Notwithstanding the potentially high experimental and computational efforts, the optical properties of multielemental alloys on its own are worth investigating, as the mixing of elements does not lead to intuitive linear combination of the properties of individual constituents. High-entropy multielemental alloyed nanoparticles can enable up to eight metals to be mixed.^[130] Therefore, we anticipate them to be a natural next-step for “fine-tuning” ϵ . By extending to multielement alloys, the materials science community could establish a massive “recipe” pool of metallic alloys for researchers to choose from for different needs, and provide a guideline for the rational design of alloy-based photonic devices.

From a computational perspective, artificial intelligence methods, such as ML, are becoming more appealing and have been recognized in the material science community over recent years^[131] as a pathway to accelerate the discovery of novel materials and to improve the performance of devices. This shift in paradigm has been inspired by their enormous impact in other research and engineering fields, such as natural language processing, autonomous vehicle and computer vision, and facilitated by the dramatic advancement of user-friendly programming tools and frameworks, such as TensorFlow, PyTorch, and Keras.^[132,133] A number of well-established algorithms in other fields have been borrowed and applied in materials science research, including support vector machine,

gradient boosting regression, and deep neural networks. Successful utilization of ML techniques in materials science-related research has been implemented in various subjects, including chiral metamaterial structure design,^[134] perovskite solar cell performance forecasting,^[135,136] battery lifetime predictions,^[137] and guidance for synthesis strategy of quantum dots.^[138] In particular, ML has lately been utilized to predict the mechanical (e.g., elastic moduli, tensile strength, etc.), thermodynamic (e.g., thermal conductivity, mixing entropy, etc.) and catalytical properties (e.g., reactant binding energy on alloy's crystalline facets) for various alloys,^[139–143] and to predict ϵ for several compound materials and polymers.^[144–147] The inverse design of alloys with targeted mechanical and electrical properties (e.g., tensile strength, conductivity, etc.) have also been realized using ML framework.^[148]

In principle, ML methods apply highly nonlinear mathematical or statistical models/algorithms/architectures, which is capable of capturing the complex relations between input (e.g., material's compositional, structural parameters) and output (e.g., material's properties of various kinds) by learning organically from the fed data during the training. This process does not directly model the underlying physical or chemical dynamics, yet the trained models can accurately reveal correlations between input “descriptors” and target output properties. Moreover, compared with conventional computational methods based on theoretical analysis or numerical simulations, or traditional trial-and-error experimental design method, a trained ML model is computationally inexpensive and extremely efficient to predict results, which can significantly accelerate the pace of material design, development, and subsequent implementation. The benefits have been extensively exemplified in a plethora of material research areas as aforementioned. In principle, the design of alloys based on optical properties is anticipated to be highly feasible, provided appropriate ML algorithms are used with proper feature engineering, hyperparameter tuning and model selection and optimization. As a result, we advocate that with sufficient amounts of optical data and properly chosen algorithm and model training and optimization processes, ML can tremendously assist in the discovery of new metallic materials, composed by the combination of—five to ten elements based on targeted optical properties.

Acknowledgements

M.S.L. acknowledges the financial support from the National Science Foundation (DMR Award Nos. #16-09414 and #20-16617) and UC Davis. K.J.P. was supported by a National Defense Science and Engineering Graduate Fellowship. S.M. thanks the financial support from Graduate School Summer Research Fellowship – University of Maryland. J.N.M. acknowledges funding from the National Science Foundation CAREER Grant No. ECCS-1554503, the Office of Naval Research YIP Award under Grant No. N00014-16-1-2540, Google LLC, and UC Davis. This article is part of the *Advanced Optical Materials* Hall of Fame article series, which recognizes the excellent contributions of leading researchers to the field of optical materials science.

Conflict of Interest

The authors declare no conflict of interest.

Keywords

alloyed nanostructures, dynamic optics, permittivity, photonics, plasmonics, thin films

Received: June 25, 2020
Revised: August 20, 2020
Published online:

- [1] M. R. S. Dias, M. S. Leite, *Acc. Chem. Res.* **2019**, *52*, 2881.
- [2] C. Gong, M. S. Leite, *ACS Photonics* **2016**, *3*, 507.
- [3] F. A. A. Nugroho, B. Iandolo, J. B. Wagner, C. Langhammer, *ACS Nano* **2016**, *10*, 2871.
- [4] Y. Nishijima, S. Shimizu, K. Kurihara, Y. Hashimoto, H. Takahashi, A. Balcytis, G. Seniutinas, S. Okazaki, J. Juodkazyte, T. Iwasa, T. Taketsugu, Y. Tominaga, S. Juodkazyte, *Opt. Express* **2017**, *25*, 24081.
- [5] K. S. De Silva, V. J. Keast, A. Gentle, M. B. Cortie, *Nanotechnology* **2017**, *28*, 095202.
- [6] V. G. Kravets, A. V. Kabashin, W. L. Barnes, A. N. Grigorenko, *Chem. Rev.* **2018**, *118*, 5912.
- [7] V. Giannini, A. I. Fernandez-Dominguez, S. C. Heck, S. A. Maier, *Chem. Rev.* **2011**, *111*, 3888.
- [8] A. I. Fernandez-Dominguez, F. J. Garcia-Vidal, L. Martin-Moreno, *Nat. Photonics* **2017**, *11*, 8.
- [9] J. N. Munday, H. A. Atwater, *Nano Lett.* **2011**, *11*, 2195.
- [10] J. Li, S. K. Cushing, F. Meng, T. R. Senty, A. D. Bristow, N. Wu, *Nat. Photonics* **2015**, *9*, 601.
- [11] Y. H. Jang, Y. J. Jang, S. Kim, L. N. Quan, K. Chung, D. H. Kim, *Chem. Rev.* **2016**, *116*, 14982.
- [12] P. Christopher, H. Xin, S. Linic, *Nat. Chem.* **2011**, *3*, 467.
- [13] S. C. Warren, E. Thimsen, *Energy Environ. Sci.* **2012**, *5*, 5133.
- [14] L. Liu, S. Ouyang, J. Ye, *Angew. Chem., Int. Ed.* **2013**, *52*, 6689.
- [15] S. Aksu, A. E. Cetin, R. Adato, H. Altug, *Adv. Opt. Mater.* **2013**, *1*, 798.
- [16] X. Deng, L. Li, M. Enomoto, Y. Kawano, *Sci. Rep.* **2019**, *9*, 3498.
- [17] A. Emboras, J. Niegemann, P. Ma, C. Haffner, A. Pedersen, M. Luisier, C. Hafner, T. Schimmel, J. Leuthold, *Nano Lett.* **2016**, *16*, 709.
- [18] C. Haffner, D. Chelladurai, Y. Fedoryshyn, A. Josten, B. Baeuerle, W. Heni, T. Watanabe, T. Cui, B. Cheng, S. Saha, D. L. Elder, L. R. Dalton, A. Boltasseva, V. M. Shalaev, N. Kinsey, J. Leuthold, *Nature* **2018**, *556*, 483.
- [19] M. R. S. Dias, C. Gong, Z. A. Benson, M. S. Leite, *Adv. Opt. Mater.* **2018**, *6*, 1700830.
- [20] H. Wang, L. Wang, *Opt. Express* **2013**, *21*, A1078.
- [21] K. Chen, T. D. Dao, S. Ishii, M. Aono, T. Nagao, *Adv. Funct. Mater.* **2015**, *25*, 6637.
- [22] I. Darmadi, F. A. A. Nugroho, S. Kadkhodazadeh, J. B. Wagner, C. Langhammer, *ACS Sens.* **2019**, *4*, 1424.
- [23] M. W. Knight, N. S. King, L. Liu, H. O. Everitt, P. Nordlander, N. J. Halas, *ACS Nano* **2014**, *8*, 834.
- [24] Q. Hao, C. Wang, H. Huang, W. Li, D. Du, D. Han, T. Qiu, P. K. Chu, *Sci. Rep.* **2015**, *5*, 15288.
- [25] X. Duan, S. Kamin, N. Liu, *Nat. Commun.* **2017**, *8*, 14606.
- [26] T. G. Farinha, C. Gong, Z. A. Benson, M. S. Leite, *ACS Photonics* **2019**, *6*, 272.
- [27] L. J. Kraye, E. M. Tennyson, M. S. Leite, J. N. Munday, *ACS Photonics* **2018**, *5*, 306.
- [28] J. J. Carr, *Microwave & Wireless Communications Technology*, Newnes, London **1996**.
- [29] H. W. Mertz, *J. SMPTE* **1962**, *71*, 872.
- [30] W. E. Kock, *Bell Syst. Tech. J.* **1948**, *27*, 58.
- [31] M. M. Z. Kharadly, W. Jackson, *Proc. Inst. Electr. Eng.* **1953**, *100*, 199.
- [32] S. G. Kwon, G. Krylova, P. J. Phillips, R. F. Klie, S. Chattopadhyay, T. Shibata, E. E. Bunel, Y. Z. Liu, V. B. Prakapenka, B. Lee, E. V. Shevchenko, *Nat. Mater.* **2015**, *14*, 215.
- [33] K. D. Gilroy, A. Ruditskiy, H. C. Peng, D. Qin, Y. N. Xia, *Chem. Rev.* **2016**, *116*, 10414.
- [34] C. Gong, M. R. S. Dias, G. C. Wessler, J. A. Taillon, L. G. Salamanca-Riba, M. S. Leite, *Adv. Opt. Mater.* **2017**, *5*, 1600568.
- [35] R. Collette, Y. Wu, A. Olafsson, J. P. Camden, P. D. Rack, *ACS Comb. Sci.* **2018**, *20*, 633.
- [36] Z. A. Benson, C. Gong, M. S. Leite, in *Metal Nanostructures for Photonics* (Eds: L. R. P. Kassab, C. B. de Araujo), Elsevier, New York **2019**, p. 87.
- [37] P. Pandey, S. Kunwar, M. Sui, S. Bastola, J. Lee, *Nanoscale Res. Lett.* **2018**, *13*, 151.
- [38] M. Sui, S. Kunwar, P. Pandey, S. Pandit, J. Lee, *New J. Phys.* **2019**, *21*, 113049.
- [39] D. Kim, A. L. Giermann, C. V. Thompson, *Appl. Phys. Lett.* **2009**, *95*, 251903.
- [40] S. Verma, B. T. Rao, A. P. Detty, V. Ganesan, D. M. Phase, S. K. Rai, A. Bose, S. C. Joshi, L. M. Kukreja, *J. Appl. Phys.* **2015**, *117*, 133105.
- [41] C. C. Tyson, A. Bzowski, P. Kristof, M. Kuhn, R. Sammynaiken, T. K. Sham, *Phys. Rev. B* **1992**, *45*, 8924.
- [42] P.-C. Chen, G. Liu, Y. Zhou, K. A. Brown, N. Chernyak, J. L. Hedrick, S. He, Z. Xie, Q.-Y. Lin, V. P. Dravid, S. A. O'Neill-Slawecki, C. A. Mirkin, *J. Am. Chem. Soc.* **2015**, *137*, 9167.
- [43] S. Kadkhodazadeh, F. A. A. Nugroho, C. Langhammer, M. Beleggia, J. B. Wagner, *ACS Photonics* **2019**, *6*, 779.
- [44] M. M. P. Arnob, F. Zhao, J. Li, W.-C. Shih, *ACS Photonics* **2017**, *4*, 1870.
- [45] G. Mattei, *Nucl. Instrum. Methods Phys. Res., Sect. B* **2002**, *191*, 323.
- [46] P. C. Wu, T.-H. Kim, A. Suvorova, M. Giangregorio, M. Saunders, G. Bruno, A. S. Brown, M. Losurdo, *Small* **2011**, *7*, 751.
- [47] Y. Chen, K. Bi, Q. Wang, M. Zheng, Q. Liu, Y. Han, J. Yang, S. Chang, G. Zhang, H. Duan, *ACS Nano* **2016**, *10*, 11228.
- [48] P. Xie, Y. Yao, Z. Huang, Z. Liu, J. Zhang, T. Li, G. Wang, R. Shahbazian-Yassar, L. Hu, C. Wang, *Nat. Commun.* **2019**, *10*, 4011.
- [49] S. Neretina, R. A. Hughes, K. D. Gilroy, M. Hajfathalian, *Acc. Chem. Res.* **2016**, *49*, 2243.
- [50] J. Rivory, *Phys. Rev. B* **1977**, *15*, 3119.
- [51] W. Ingram, S. Larson, D. Carlson, Y. Zhao, *Nanotechnology* **2017**, *28*, 015301.
- [52] D. J. McPherson, S. Supansomboon, B. Zwan, V. J. Keast, D. L. Cortie, A. Gentle, A. Dowd, M. B. Cortie, *Thin Solid Films* **2014**, *551*, 200.
- [53] *Alloy Phase Diagrams*, ASM International, Materials Park, OH **2016**.
- [54] D. Rioux, S. Vallières, S. Besner, P. Muñoz, E. Mazur, M. Meunier, *Adv. Opt. Mater.* **2014**, *2*, 176.
- [55] K. Appusamy, M. Swartz, S. Blair, A. Nahata, J. S. Shumaker-Parry, S. Guruswamy, *Opt. Mater. Express* **2016**, *6*, 3180.
- [56] M. H. Chiu, J. H. Li, T. Nagao, *Micromachines* **2019**, *10*, 73.
- [57] V. Amendola, S. Scaramuzza, S. Agnoli, S. Polizzi, M. Meneghetti, *Nanoscale* **2014**, *6*, 1423.
- [58] P. Mohan, M. Takahashi, K. Higashimine, D. Mott, S. Maenosono, *Langmuir* **2017**, *33*, 1687.
- [59] C. F. Bohren, D. R. Huffman, *Absorption and Scattering of Light by Small Particles*, Wiley-Interscience, New York **1983**.
- [60] B. T. Draine, P. J. Flatau, *J. Opt. Soc. Am. A* **2008**, *25*, 2693.
- [61] H. G. Tompkins, S. Tasic, J. Baker, D. Convey, *Surf. Interface Anal.* **2000**, *29*, 179.
- [62] M. B. Cortie, M. D. Arnold, V. J. Keast, *Adv. Mater.* **2020**, *32*, 1904532.
- [63] G. Meng, R. Claessen, F. Reinert, R. Zimmermann, P. Steiner, S. Hüfner, *J. Phys.: Condens. Matter* **1996**, *8*, 5569.
- [64] K. S. B. De Silva, V. J. Keast, M. B. Cortie, *J. Alloys Compd.* **2016**, *679*, 225.

- [65] V. J. Keast, R. L. Barnett, M. B. Cortie, *J. Phys.: Condens. Matter* **2014**, *26*, 305501.
- [66] D. A. Bobb, G. Zhu, M. Mayy, A. V. Gavrilenko, P. Mead, V. I. Gavrilenko, M. A. Noginov, *Appl. Phys. Lett.* **2009**, *95*, 151102.
- [67] N. Shahcheraghi, V. J. Keast, A. R. Gentle, M. D. Arnold, M. B. Cortie, *J. Phys.: Condens. Matter* **2016**, *28*, 405501.
- [68] L. J. Kraye, K. J. Palm, C. Gong, A. Torres, C. E. P. Villegas, A. R. Rocha, M. S. Leite, J. N. Munday, *ACS Photonics* **2020**, *7*, 1689.
- [69] L. J. Kraye, J. Kim, J. L. Garrett, J. N. Munday, *ACS Photonics* **2019**, *6*, 2238.
- [70] M. A. Kats, R. Blanchard, P. Genevet, F. Capasso, *Nat. Mater.* **2013**, *12*, 20.
- [71] C. Ambrosch-Draxl, J. O. Sofo, *Comput. Phys. Commun.* **2006**, *175*, 1.
- [72] J. M. Rahm, C. Tiburski, T. P. Rossi, F. A. A. Nugroho, S. Nilsson, C. Langhammer, P. Erhart, *Adv. Funct. Mater.* **2020**, *30*, 2002122.
- [73] M. Moskovits, I. Srnova-Sloufova, B. Vlckova, *J. Chem. Phys.* **2002**, *116*, 10435.
- [74] N. Kinsey, C. DeVault, A. Boltasseva, V. M. Shalaev, *Nat. Rev. Mater.* **2019**, *4*, 742.
- [75] M. Gaudry, J. Lermé, E. Cottancin, M. Pellarin, J. L. Vialle, M. Broyer, B. Prével, M. Treilleux, P. Mélinon, *Phys. Rev. B* **2001**, *64*, 085407.
- [76] Y. Hashimoto, G. Seniutinas, A. Balcytis, S. Juodkazis, Y. Nishijima, *Sci. Rep.* **2016**, *6*, 25010.
- [77] V. I. Belotelov, G. Carotenuto, L. Nicolais, A. Longo, G. P. Pepe, P. Perlo, A. K. Zvezdin, *J. Appl. Phys.* **2006**, *99*, 044304.
- [78] V. J. Keast, K. Birt, C. T. Koch, S. Supansomboon, M. B. Cortie, *Appl. Phys. Lett.* **2011**, *99*, 111908.
- [79] V. J. Keast, B. Zwan, S. Supansomboon, M. B. Cortie, P. O. Å. Persson, *J. Alloys Compd.* **2013**, *577*, 581.
- [80] C. Gong, A. Kaplan, Z. A. Benson, D. R. Baker, J. P. McClure, A. R. Rocha, M. S. Leite, *Adv. Opt. Mater.* **2018**, *6*, 1800218.
- [81] A. P. Vinogradov, A. V. Dorofeenko, A. A. Pukhov, A. A. Lisyansky, *Phys. Rev. B* **2018**, *97*, 235407.
- [82] P. G. Etchegoin, E. C. Le Ru, M. Meyer, *J. Chem. Phys.* **2006**, *125*, 164705.
- [83] J. P. McClure, J. Boltersdorf, D. R. Baker, T. G. Farinha, N. Dzuricky, C. E. P. Villegas, A. R. Rocha, M. S. Leite, *ACS Appl. Mater. Interfaces* **2019**, *11*, 24919.
- [84] N. I. Landy, S. Sajuyigbe, J. J. Mock, D. R. Smith, W. J. Padilla, *Phys. Rev. Lett.* **2008**, *100*, 207402.
- [85] S. T. Yen, P. K. Chung, *Opt. Lett.* **2015**, *40*, 3877.
- [86] A. Manjavacas, J. G. Liu, V. Kulkarni, P. Nordlander, *ACS Nano* **2014**, *8*, 7630.
- [87] F. M. Wang, N. A. Melosh, *Nano Lett.* **2011**, *11*, 5426.
- [88] W. Li, J. G. Valentine, *Nanophotonics* **2017**, *6*, 177.
- [89] T. Gong, J. N. Munday, *Opt. Mater. Express* **2015**, *5*, 2501.
- [90] S. Memarzadeh, J. Kim, Y. Aytac, T. E. Murphy, J. N. Munday, *Optica* **2020**, *7*, 608.
- [91] M. N. Su, C. J. Ciccarino, S. Kumar, P. D. Dongare, S. A. Hosseini Jebeli, D. Renard, Y. Zhang, B. Ostovar, W. S. Chang, P. Nordlander, N. J. Halas, R. Sundararaman, P. Narang, S. Link, *Nano Lett.* **2019**, *19*, 3091.
- [92] S. Memarzadeh, K. J. Palm, T. E. Murphy, M. S. Leite, J. N. Munday, arXiv preprint arXiv:2007.15561, **2020**.
- [93] F. A. A. Nugroho, I. Darmadi, L. Cusinato, A. Susarrey-Arce, H. Schreuders, L. J. Bannenberg, A. B. D. Fanta, S. Kadkhodazadeh, J. B. Wagner, T. J. Antosiewicz, A. Hellman, V. P. Zhdanov, B. Dam, C. Langhammer, *Nat. Mater.* **2019**, *18*, 489.
- [94] K. J. Palm, J. B. Murray, J. P. McClure, M. S. Leite, J. N. Munday, *ACS Appl. Mater. Interfaces* **2019**, *11*, 45057.
- [95] H. K. Deepti, A. Tripathi, A. B. Dey, M. Gupta, R. Krishna, D. K. Avasthi, *Sens. Actuators, B* **2019**, *307*, 127006.
- [96] R. J. Westerwaal, J. S. A. Rooijmans, L. Leclercq, D. G. Gheorghe, T. Radeva, L. Mooij, T. Mak, L. Polak, M. Slaman, B. Dam, T. Rasing, *Int. J. Hydrogen Energy* **2013**, *38*, 4201.
- [97] Y. Debauge, M. Abon, J. C. Bertolini, J. Massardier, A. Rochefort, *Appl. Surf. Sci.* **1995**, *90*, 15.
- [98] K. J. Palm, J. B. Murray, T. C. Narayan, J. N. Munday, *ACS Photonics* **2018**, *5*, 4677.
- [99] Y. Yamada, S. Bao, K. Tajima, M. Okada, K. Yoshimura, *Appl. Phys. Lett.* **2009**, *94*, 191910.
- [100] D. M. Borsa, A. Baldi, M. Pasturel, H. Schreuders, B. Dam, R. Griessen, P. Vermeulen, P. H. L. Notten, *Appl. Phys. Lett.* **2006**, *88*, 241910.
- [101] I. A. M. E. Giebels, J. Isidorsson, R. Griessen, *Phys. Rev. B* **2004**, *69*, 205111.
- [102] J. L. M. van Mechelen, B. Noheda, W. Lohstroh, R. J. Westerwaal, J. H. Rector, B. Dam, R. Griessen, *Appl. Phys. Lett.* **2004**, *84*, 3651.
- [103] P. Wang, B. B. Huang, Y. Dai, M. H. Whangbo, *Phys. Chem. Chem. Phys.* **2012**, *14*, 9813.
- [104] Z. L. Zhang, C. Y. Zhang, H. R. Zheng, H. X. Xu, *Acc. Chem. Res.* **2019**, *52*, 2506.
- [105] I. Sarhid, I. Abdellah, C. Martini, V. Hu, D. Dragoe, P. Beaunier, I. Lampre, H. Remita, *New J. Chem.* **2019**, *43*, 4349.
- [106] K. Sivula, R. van de Krol, *Nat. Rev. Mater.* **2016**, *1*, 15010.
- [107] M. Valenti, A. Venugopal, D. Tordera, M. P. Jonsson, G. Biskos, A. Schmidt-Ott, W. A. Smith, *ACS Photonics* **2017**, *4*, 1146.
- [108] S. Chattopadhyay, S. Bysakh, P. M. Mishra, G. De, *Langmuir* **2019**, *35*, 14364.
- [109] M. Hartings, *Nat. Chem.* **2012**, *4*, 764.
- [110] K. Yamada, K. Miyajima, F. Mafune, *J. Phys. Chem. C* **2007**, *111*, 11246.
- [111] S. Sarina, H. Zhu, E. Jaatinen, Q. Xiao, H. Liu, J. Jia, C. Chen, J. Zhao, *J. Am. Chem. Soc.* **2013**, *135*, 5793.
- [112] Q. Xiao, S. Sarina, E. R. Waclawik, J. F. Jia, J. Chang, J. D. Riches, H. S. Wu, Z. F. Zheng, H. Y. Zhu, *ACS Catal.* **2016**, *6*, 1744.
- [113] T. T. Jiang, C. C. Jia, L. C. Zhang, S. R. He, Y. H. Sang, H. D. Li, Y. Q. Li, X. H. Xu, H. Liu, *Nanoscale* **2015**, *7*, 209.
- [114] S. Peiris, S. Sarina, C. Han, Q. Xiao, H. Y. Zhu, *Dalton Trans.* **2017**, *46*, 10665.
- [115] S. K. Movahed, S. Miraghaee, M. Dabiri, *J. Alloys Compd.* **2020**, *819*, 152994.
- [116] S. C. Hsu, Y. C. Chuang, B. T. Sneed, D. A. Cullen, T. W. Chiu, C. H. Kuo, *Nano Lett.* **2016**, *16*, 5514.
- [117] I. Katsounaros, S. Cherevko, A. R. Zeradjanin, K. J. J. Mayrhofer, *Angew. Chem., Int. Ed.* **2014**, *53*, 102.
- [118] S. C. Lin, C. S. Hsu, S. Y. Chiu, T. Y. Liao, H. M. Chen, *J. Am. Chem. Soc.* **2017**, *139*, 2224.
- [119] Z. Li, Y. Li, C. He, P. K. Shen, *J. Mater. Chem. A* **2017**, *5*, 23158.
- [120] A. Kojima, K. Teshima, Y. Shirai, T. Miyasaka, *J. Am. Chem. Soc.* **2009**, *131*, 6050.
- [121] S. Carretero-Palacios, A. Jimenez-Solano, H. Miguez, *ACS Energy Lett.* **2016**, *1*, 323.
- [122] Z. Lu, X. Pan, Y. Ma, Y. Li, L. Zheng, D. Zhang, Q. Xu, Z. Chen, S. Wang, B. Qu, F. Liu, Y. Huang, L. Xiao, Q. Gong, *RSC Adv.* **2015**, *5*, 11175.
- [123] T. W. Hamann, R. A. Jensen, A. B. F. Martinson, H. Van Ryswyk, J. T. Hupp, *Energy Environ. Sci.* **2008**, *1*, 66.
- [124] Q. Xu, F. Liu, Y. Liu, K. Cui, X. Feng, W. Zhang, Y. Huang, *Sci. Rep.* **2013**, *3*, 2112.
- [125] S. Morawiec, M. J. Mendes, S. Mirabella, F. Simone, F. Priolo, I. Crupi, *Nanotechnology* **2013**, *24*, 265601.
- [126] S. K. Sardana, V. K. Komarala, *J. Opt.* **2016**, *18*, 075004.
- [127] P. K. Parashar, V. K. Komarala, *Sci. Rep.* **2017**, *7*, 12520.
- [128] M. A. Asoro, D. Kovar, P. J. Ferreira, *ACS Nano* **2013**, *7*, 7844.
- [129] J. Gao, X. Wang, B. Yang, C. Tu, L. Liang, H. Zhang, F. Zhuge, H. Cao, Y. Zou, K. Yu, F. Xia, Y. Han, *Adv. Mater. Interfaces* **2016**, *3*, 1600248.
- [130] M. H. Tsai, J. W. Yeh, *Mater. Res. Lett.* **2014**, *2*, 107.
- [131] K. T. Butler, D. W. Davies, H. Cartwright, O. Isayev, A. Walsh, *Nature* **2018**, *559*, 547.

- [132] N. Ketkar, in *Deep Learning with Python: A Hands-on Introduction* (Ed: N. Ketkar), Apress, Berkeley, CA **2017**, p. 195.
- [133] M. Abadi, P. Barham, J. Chen, Z. Chen, A. Davis, J. Dean, M. Devin, S. Ghemawat, G. Irving, M. Isard, M. Kudlur, J. Levenberg, R. Monga, S. Moore, D. G. Murray, B. Steiner, P. Tucker, V. Vasudevan, P. Warden, M. Wicke, Y. Yu, X. Zheng, in *Proc. USENIX Symp. on Operating Systems Design and Implementation*, USENIX Association, Savannah, GA **2016**.
- [134] W. Ma, F. Cheng, Y. Liu, *ACS Nano* **2018**, *12*, 6326.
- [135] K. Takahashi, L. Takahashi, I. Miyazato, Y. Tanaka, *ACS Photonics* **2018**, *5*, 771.
- [136] J. M. Howard, E. M. Tennyson, B. R. A. Neves, M. S. Leite, *Joule* **2019**, *3*, 325.
- [137] K. A. Severson, P. M. Attia, N. Jin, N. Perkins, B. Jiang, Z. Yang, M. H. Chen, M. Aykol, P. K. Herring, D. Fraggedakis, M. Z. Bazan, S. J. Harris, W. C. Chueh, R. D. Braatz, *Nat. Energy* **2019**, *4*, 383.
- [138] O. Voznyy, L. Levina, J. Z. Fan, M. Askerka, A. Jain, M. J. Choi, O. Ouellette, P. Todorovic, L. K. Sagar, E. H. Sargent, *ACS Nano* **2019**, *13*, 11122.
- [139] J. Xiong, S.-Q. Shi, T.-Y. Zhang, *Mater. Des.* **2020**, *187*, 108378.
- [140] Z. Pei, J. Yin, J. A. Hawk, D. E. Alman, M. C. Gao, *npj Comput. Mater.* **2020**, *6*, 50.
- [141] Z. Yang, W. Gao, Q. Jiang, *J. Mater. Chem. A* **2020**, *8*, 17507.
- [142] Z.-h. Deng, H.-q. Yin, X. Jiang, C. Zhang, G.-f. Zhang, B. Xu, G.-q. Yang, T. Zhang, M. Wu, X.-h. Qu, *Int. J. Miner. Metall. Mater.* **2020**, *27*, 362.
- [143] G. Liu, L. Jia, B. Kong, S. Feng, H. Zhang, H. Zhang, *Mater. Sci. Eng. A* **2017**, *707*, 452.
- [144] Y. Umeda, H. Hayashi, H. Moriwake, I. Tanaka, *Jpn. J. Appl. Phys.* **2019**, *58*, SLLC01.
- [145] L. Chen, C. Kim, R. Batra, J. P. Lightstone, C. Wu, Z. Li, A. A. Deshmukh, Y. Wang, H. D. Tran, P. Vashishta, G. A. Sotzing, Y. Cao, R. Ramprasad, *npj Comput. Mater.* **2020**, *6*, 61.
- [146] K. Morita, D. W. Davies, K. T. Butler, A. Walsh, *J. Chem. Phys.* **2020**, *153*, 024503.
- [147] L. Zhang, M. Chen, X. Wu, H. Wang, W. E. R. Car, *Phys. Rev. B* **2020**, *102*, 041121.
- [148] C. Wang, H. Fu, L. Jiang, D. Xue, J. Xie, *npj Comput. Mater.* **2019**, *5*, 87.



Tao Gong is currently a postdoc researcher at the University of California, Davis. He obtained his B.S. degree in physics at the University of Science and Technology of China in 2011, and his Ph.D. degree in electrical engineering at the University of Maryland, College Park in 2016 and worked as an engineer at MathWorks thereafter. His current research interest covers novel plasmonic and nanophotonic materials, Casimir force, and machine learning-based study on perovskite photovoltaics.



Marina S. Leite is an associate professor in the Department of Materials Science and Engineering at the University of California, Davis. She received her Ph.D. in Physics from Campinas State University, in Brazil. Her group is engaged in fundamental and applied research on functional materials, including the development of metallic thin films and nanostructures with engineered optical behavior for photonics and plasmonics.